Open access • Journal Article • DOI:10.1088/1361-6463/50/2/023001

Exploring the potential of semiconducting BaSi2 for thin-film solar cell applications

Takashi Suemasu, Noritaka Usami

Institutions: University of Tsukuba, Nagoya University

Published on: 18 Jan 2017 - Journal of Physics D (IOP Publishing)

Topics: Thin film

Exploring the Potential of Semiconducting $BaSi_2$ for Thin-Film Solar Cell Applications

Takashi Suemasu[1] and Noritaka Usami[2]

[1] *Institute of Applied Physics, University of Tsukuba, Tsukuba, Ibaraki 305-8573, Japan*

[2] *Graduate School of Engineering, Nagoya University, Nagoya 464-8063, Japan*

Semiconducting barium disilicide ($BaSi_2$), which is composed of earth-abundant elements, has attractive features for thin-film solar cell applications; both a large absorption coefficient comparable to copper indium gallium diselenide and a minority-carrier diffusion length much larger than the grain size of $BaSi_2$ can be used to improve solar cells properties. In this review article, we explore the potential of semiconducting $BaSi_2$ films for thin-film solar cell applications. We start by describing its crystal and energy band structure, followed by discussing thin-film growth techniques and the optical and electrical properties of $BaSi_2$ films. We used a first-principle calculation based on density-functional theory to calculate the position of the Fermi level to predict the carrier type of impurity-doped $BaSi_2$ films using either a Group 13 or 15 element, and compare the calculated results with the experimental ones. Special attention was paid to the minority-carrier properties, such as minority-carrier lifetime, minority-carrier diffusion length, and surface passivation. The potential variations across the grain boundaries measured by Kelvin-probe force microscopy allowed us to

detect a larger minority-carrier diffusion length in $BaSi_2$ on Si(111) compared with in $BaSi_2$ on Si(001). Finally, we demonstrate the operation of p-$BaSi_2$/n-Si heterojunction solar cells and discuss prospects for future development.

1. Introduction

1.1 Thin-film solar cell materials: alternatives to Si

A solar cell, which converts sunlight directly into electrical energy, is the primary device for photovoltaics (PV). PV systems have been rapidly and globally deployed and reached a cumulative installed capacity of over 200 GWp in 2015. However, it is necessary to further deploy PV systems to establish a sustainable energy supply while also avoiding the various environmental and safety issues related to burning fossil fuels and nuclear power plants. For this purpose, a reduction of the energy costs per watt-peak must be pursued based on improving the energy conversion efficiency of solar cells and decreasing manufacturing costs.

At the moment, more than 90% of installed solar cells are based on crystalline silicon, and a large-scale production system for PV modules based on crystalline silicon solar cells is well established. Silicon is safe, stable, and earth-abundant, and crystalline silicon solar cells will continue to play an important role for the sustainable supply of energy in the near future.

However, there are two main drawbacks to using crystalline silicon. One drawback is that silicon is an indirect band-gap semiconductor, which leads to it having a relatively low absorption coefficient. To efficiently absorb sunlight the wafer must therefore be thick,

and the average wafer thickness for commercially available solar cells amounts to ~180 μm. Although further reduction in the wafer thickness to ~100 μm in 2023 is predicted [1], there will be a lot of technical challenges. Even if one can reduce the wafer thickness down to 100 μm, silicon wafers will still account for the majority of the cell's price and thus the thickness reduction will not have a drastic impact on decreasing manufacturing costs.

Another drawback is the width of its band gap. The band gap of silicon (1.1 eV) is slightly narrower compared with the ideal band gap (~1.4 eV) for a single-junction solar cell. Kaneka recently reported a record efficiency of 26.33% using a back-contact heterojunction crystalline silicon solar cell by utilizing advanced processing [2]. The achieved efficiency is already very close to the theoretical Shockley-Queisser limit [3] for a 1.1 eV band gap, and thus there is little room for further improvement in this regard.

To overcome the drawbacks of silicon, thin film solar cells using alternative materials with wider band gaps have been intensively studied and developed; for example, cadmium telluride (CdTe) and copper indium gallium diselenide (CIGS) thin film solar cells have already been commercialized. However, these materials lack some important properties for global deployment, which will make it difficult for them to become market leaders. Solar cell materials should be safe, stable, and earth-abundant like silicon. The

ideal alternative absorber material for thin film solar cells should have a high absorption coefficient, long minority carrier lifetime, and band gap close to 1.4 eV. Orthorhombic barium disilicide ($BaSi_2$) has all these properties, which will be described in the following sections.

1.2 Crystal structure and energy band structure

Orthorhombic $BaSi_2$ (lattice constants: $a = 0.891$ nm, $b = 0.672$ nm, $c = 1.153$ nm) is in a stable phase at room temperature (RT) and under atmospheric pressure [4–6]. The unit cell of $BaSi_2$ is shown in Fig. 1. There are two crystallographically inequivalent sites for Ba ($Ba^{(1)}$ and $Ba^{(2)}$) and three inequivalent sites for Si ($Si^{(3)}$, $Si^{(4)}$, and $Si^{(5)}$). The unit cell contains eight formula units. Therefore, the stoichiometric description of the unit cell is Ba_8Si_{16}, and the atoms are distributed over $4Ba^{(1)}$, $4Ba^{(2)}$, $4Si^{(3)}$, $4Si^{(4)}$, and $8Si^{(5)}$. In a Si tetrahedron, each Si atom forms four sp^3 hybridized orbitals and connects with three other Si atoms, leaving one external sp^3 orbital as a dangling bond. The four dangling bonds associated with each Si tetrahedron are thought to be filled with four electrons donated by two Ba atoms. In this way, each Si atom is associated with eight electrons. It is therefore safe to say that there are strong covalent bonds between the Si atoms via the sp^3 hybridized orbitals in addition to ionic bonding between Ba and Si in the tetrahedron, although the Ba-Si bonds will have some covalent characteristics. The Ba atoms situated

between the Si tetrahedra can therefore be regarded as working to connect the Si tetrahedra. First-principle calculations of the band structure of $BaSi_2$ have been carried out [7–11]. Figs. 2(a) and 2(b) show the partial densities of states (DOS) of Si *s*, *p*, and Ba *s*, *p*, and *d* states, and their energy band structures, respectively, which were determined using VASP code [12] based on density-functional theory (DFT) using the projector-augmented wave pseudopotential [13] and Perdew-Wang Generalized Gradient Approximations method [14]. The total energy minimization was obtained via an optimization of the lattice parameters and a relaxation of the atomic positions in a conjugate gradient routine. The convergence in total energy was better than 1 meV/atom using an energy cutoff of 600 eV and a 6 × 8 × 4 grid of Monkhorst–Pack points [15]. We cannot take thermal effects at a finite temperature into account in our framework of first-principle DFT calculations. The Si *p* state appears dominant in the valence band maximum (VBM), while the conduction band minimum (CBM) mainly consists of the Ba *d* state [7], leading to large values of the dipole matrix elements [8–10]. The CBM is located at T(0, 1/2, 1/2), and the VBM is located at approximately (0, 1/3, 0) along the Γ–Y(0, 1/2, 0) direction, as shown in Fig. 2(b). A direct transition occurs at approximately (0, 1/3, 0), and its gap value is higher than the band gap by approximately 0.1 eV. This might be the reason why experimental studies have revealed that $BaSi_2$ has high

absorption coefficients in spite of its indirect band gap nature [16,17]. The effective mass for electrons and for holes are 0.41 and 0.53, respectively [9]. The effective density of states in conduction band and that in valence band is calculated to be 2.6×10^{19} cm^{-3} and 2.0×10^{19} cm^{-3}, respectively. Both theoretical and experimental studies have revealed that it has a band gap of approximately 1.3 eV [10,16,17] and has high absorption coefficients (α) exceeding 3×10^4 cm^{-1} for photon energies higher than 1.5 eV [17]. Recent experimental results demonstrating a large minority-carrier diffusion length (L ~10 μm) [18,19], a long minority-carrier lifetime (τ ~10 μs) [20-22], and potential variations across grain boundaries (GBs) [23] in $BaSi_2$ confirm that this material is a new candidate for thin-film solar cells. The obtained values of α, L, and τ (described later) are sufficiently large for thin-film solar cell applications.

2. Formation of $BaSi_2$ films

The formation of high-quality $BaSi_2$ films is very important for device applications. Epitaxial growth of $BaSi_2$ films was first reported by Mckees *et al*. We note here that [100]-oriented $BaSi_2$ can be grown on the (001) and (111) faces of Si substrates by reactive deposition epitaxy (RDE; Ba deposition on hot Si) [24] and solid-phase epitaxy (SPE; Ba deposition on Si at RT with subsequent annealing) [25]. $BaSi_2$(100) is a better

match for the Si(111) over the Si(001) face for $BaSi_2$[001]//Si[1-10]. The lattice mismatch is only 1.1% for Si(111) while it is more than 10% for Si(001). In this article, we introduce three methods to grow $BaSi_2$ films thicker than 1 μm, namely molecular beam epitaxy (MBE), vacuum evaporation, and sputtering, as described in sections 2.1, 2.2, and 2.3, respectively.

2.1 Molecular beam epitaxy

An ion-pumped MBE system equipped with an electron-beam evaporation source for Si and a standard Knudsen cell (K-cell) for Ba is used. We use a two-step growth method including RDE to form epitaxial templates and MBE (Ba and Si codeposition) on Si(111) [26,27] and Si(001) [28], as shown in Fig. 3. Templates act as a kind of seed crystal for overlayers, owing to which *a*-axis-oriented epitaxial layers of $BaSi_2$ can be grown over a wide temperature range from 450 to 700 ºC [27]. The thickness of a $BaSi_2$ film by RDE is calculated using the theoretical densities of Ba, Si, and $BaSi_2$; 1 nm of Ba reacts with 0.63 nm of Si, resulting in 1.38 nm of $BaSi_2$. A substrate temperature T_S of approximately 580 ºC is optimal for MBE to achieve the highest crystalline quality $BaSi_2$ films [29]. The $BaSi_2$ deposition rate is approximately 1 nm/min. Note that *a*-axis-oriented $BaSi_2$ layers are not single crystalline, but are instead multi-domain epitaxial layers. Fig. 4, panels (a) and (a') through to (e) and (e') show examples of the reflection high-energy electron

diffraction (RHEED) pattern, θ-2θ XRD pattern with Cu Kα radiation, X-ray pole figure using asymmetric $BaSi_2$(301) and (203) diffractions, electron backscatter diffraction (EBSD), and schematics of epitaxial variants of *a*-axis-oriented $BaSi_2$ epitaxial layers grown on Si(111) and Si(001), respectively. In spite of three epitaxial variants on Si(111), the RHEED pattern is streaky, as shown in Fig. 4(a) [30]. In contrast, as shown in Fig. 4(a'), we observe two clear sets of streaky patterns with different spacings of the epitaxial layers on Si(001). The ratio of the wide streaky spacing to the narrow spacing is approximately 1.7, which is consistent with the ratio of 1/*b* to 1/*c*. Taking into account the fact that the electron beam was incident along the Si[-110] azimuth, these two streaky patterns with different spacings indicate the coexistence of epitaxial variants rotated by 90º [28]. Owing to the symmetry of Si(111) and Si(001) substrates, there are three or two epitaxial variants rotating around each other by 120° or 90°, respectively, in the surface normal for *a*-axis-oriented $BaSi_2$ epitaxial films, as shown in Fig. 4, panels (c) and (c') as well as (d) and (d'). The grain size of $BaSi_2$ variants can be increased by using a vicinal Si substrate [31,32] or by employing large grained RDE-grown $BaSi_2$ templates [33]. The grain size can reach approximately 9 μm and 4 μm for $BaSi_2$ on Si(001) and Si(111), respectively.

2.2 Vacuum evaporation

Vacuum evaporation is a practical method to deposit thin films on large-area substrates. The process generally consists of pumping a chamber down to ~10^{-5} Torr and heating a source material to provide a vapor flux. Unlike in MBE, an ultrahigh vacuum (UHV) is not a prerequisite, and the equipment can therefore be simple and inexpensive. The deposition rate can be several orders of magnitudes higher than MBE. These advantages, which are compatible with production technology, led us to investigate the growth of $BaSi_2$ thin films on various substrates by vacuum evaporation using air-stable $BaSi_2$ granules as a source material.

Although the equipment for vacuum evaporation is simple, the fundamental growth process is rather complicated, especially when one uses compound source materials such as $BaSi_2$. The equilibrium vapor pressure of the constituent elements of the compound can be vastly different. In addition, a chemical reaction between the source and boat materials may take place. Both these issues would lead to an inhomogeneous vaporization, and thin films resulting from such an inhomogeneous vapor are not necessarily comprised of the same compound as the source material. The possible chemical processes during the deposition of $BaSi_2$ on Si by vacuum evaporation using $BaSi_2$ source are illustrated in Fig. 5.

Nakagawa *et al.* revealed that an appropriately high T_S is crucially important to obtain

single-phase $BaSi_2$ on Si by vacuum evaporation using a $BaSi_2$ granular source [34]. Fig. 6 compares the Raman spectra of the films on Si(111) deposited at various T_S. The spectra of the films deposited at 500 °C and 600 °C are in good agreement with the reported spectrum for $BaSi_2$ [35], and multiple peaks originating from the T_d symmetry of the discrete $[Si_4]^{4-}$ anion are clearly observed. Recently, polarized Raman spectroscopy was utilized to identify each mode and new peak assignments to reflect crystal symmetry have been made [36]. Conversely, the spectra of the films deposited at 400 °C and RT contain a Si peak. No peaks from $BaSi_2$ were found for the film deposited at RT. We interpret these data as resulting from a Ba-rich vapor flux and the reaction of excess Ba and Si supplied from the substrate. Hara *et al*. analyzed the boat used for vacuum evaporation using $BaSi_2$ granules and confirmed the existence of a porous product of Si, which originates from the decomposition of $BaSi_2$, and of a tungsten silicide layer formed by a chemical reaction [37]. They are both expected to produce Ba gas, which suggests the formation of a Ba-rich vapor flux at the initial stage of the evaporation. Therefore, the resultant thin film may be considered to be Ba-rich silicide instead of stoichiometric $BaSi_2$. Interestingly, the thin film could still become $BaSi_2$ if the substrate contains Si, e.g., single crystalline Si or SiO_2, and a high enough substrate temperature is used to promote the reaction of excess Ba and Si. If the substrate temperature is not high enough, excess Ba

could be oxidized on exposure to air leaving Si, which explains why the Raman spectra showed a clear Si peak for the samples deposited at lower temperatures. The critical substrate temperature for the formation of $BaSi_2$ depends on the film thickness [38]. Si atoms to compensate excess Ba can originate from deposited Si thin films on various substrates. Hara *et al*. have shown that pre-deposited amorphous Si (a-Si) is the key to obtaining stoichiometric $BaSi_2$ thin films, and they succeeded in obtaining crack-free $BaSi_2$ thin films on CaF_2 substrates [39], which have a similar linear expansion coefficient to $BaSi_2$ [40]. Other substrates, such as stainless steel, titanium [41], and Ge [42], have been used successfully as substrates for $BaSi_2$ thin films. Although the thin films are generally polycrystalline, epitaxial growth of $BaSi_2$ on Si by vacuum evaporation could be achieved by carefully controlling the source temperature. Nakagawa *et al*. attempted to provide only Ba vapor from a $BaSi_2$ source by keeping the source current low so that the decomposition of $BaSi_2$ preferentially takes place [43]. This resulted in the formation of *a*-axis oriented $BaSi_2$, which can act as the template layer for subsequent epitaxial growth similar as for MBE.

2.3 Sputtering

Sputtering is another feasible thin-film deposition technology. There have been many studies on the formation of sputtered solar cell absorbers [44–46]. However, there has

been only one report on the formation of $BaSi_2$ films by sputtering [47]. Yang *et al*. formed polycrystalline $BaSi_2$ films on Si(111) by sputtering a Ba target at RT, followed by annealing at temperatures from 400 to 800 °C in UHV [47]. However, the grown films contained metallic phases such as Ba_2Si and Ba_5Si_3. Single-phase $BaSi_2$ can be grown on glass substrates by radio frequency (RF) sputtering using a polycrystalline $BaSi_2$ target produced by the Tosoh Corporation [48,49]. $BaSi_2$ films can be formed either by sputtering the $BaSi_2$ target at RT, followed by post-annealing at 500 °C or by sputtering it at elevated temperatures such as 600 °C. Fig. 7 shows a typical example of θ-2θ XRD patterns with Cu Kα radiation formed at different temperatures. The benefit of this method is its higher deposition rate, which exceeds 30 nm/min. Distinct photoresponse spectra were obtained for photon energies greater than the band gap [48].

3. Control of carrier type and carrier concentration by impurity doping

3.1 Intrinsically doped n-$BaSi_2$

Before going into details about impurity-doped $BaSi_2$, we first present the electrical properties of intrinsically doped n-$BaSi_2$. Intrinsically doped $BaSi_2$ shows n-type conductivity regardless of thin-film growth method. An electron concentration n varies from $n \sim 10^{16}$ cm^{-3} for MBE-grown $BaSi_2$ films [16,50] to $n > 10^{18}$ cm^{-3} for sputtered or

vacuum-evaporated $BaSi_2$ films [48,51,52]. A first-principles DFT supercell approach revealed that this n-type conductivity arises from Si vacancies [53]. Hereafter, we denote intrinsically doped n-$BaSi_2$ simply as n-$BaSi_2$. Figure 8 shows the temperature dependence of electron mobility of n-$BaSi_2$ grown by MBE. The n is 5×10^{15} cm^{-3} at 300 K [16]. The electron mobility is as large as approximately 800 cm^2/Vs at 300 K. For lower impurity concentrations, the mobility is limited by phonon scattering at high temperatures. The measured slope, however, is slightly different from –3/2 probably because of different scattering mechanism. Scattering mechanisms in $BaSi_2$ have yet to be investigated.

The basic structure of a solar cell is a pn junction. Therefore, control of the carrier type of $BaSi_2$ by impurity doping is required to create a solar cell. Impurity doping in $BaSi_2$ was first attempted experimentally using Al or In [54], followed by a first-principle calculation [55]. In this article, we first calculate the DOSs and total energies of impurity-doped $BaSi_2$ to find the position of the Fermi level, E_F, and which sites the impurity atoms are most likely to occupy in the lattice. We next describe the experimental results with regards to the carrier type and carrier concentration of impurity-doped $BaSi_2$.

3.2 Group 13 or 15 doping by first-principle calculation

As described in section 1.2, the VBM is mostly composed of the Si p state in $BaSi_2$. Hence,

we expect that the replacement of some Si atoms in $BaSi_2$ by a Group 13 (15) element will decrease (increase) the valence electron concentration and cause $BaSi_2$ to become a p- (n-) type semiconductor. We describe impurity-doped $BaSi_2$ as, for example, $Ba_8Ga^{(3)}Si_{15}$, where one of the $Si^{(3)}$ sites of Ba_8Si_{16} has been substituted with Ga. Meanwhile, $Ba_7Ga^{(1)}Si_{16}$ signifies that one of the $Ba^{(1)}$ sites has been replaced with Ga. According to Imai and Watanabe [55], the energy differences between $Ba_7Ga^{(1)}Si_{16}$ and $Ba_7Ga^{(2)}Si_{16}$ and between $Ba_8Ga^{(3)}Si_{15}$, $Ba_8Ga^{(4)}Si_{15}$, and $Ba_8Ga^{(5)}Si_{15}$ are small. The same is true for In doping [55]. In this article we therefore chose one $Ba^{(1)}$ site for Ba substitution, and one $Si^{(3)}$ site for Si substitution although there are two other Si sites, $Si^{(4)}$ and $Si^{(5)}$, and another Ba site, $Ba^{(2)}$, in Ba_8Si_{16}. Regarding the interstitial site, the most probable insertion sites are the 4*c* sites [55], where an impurity atom is surrounded by three Si atoms, one of which is at a corner of one of the Si-tetrahedrons while the other two make up one of the edges of the other Si-tetrahedron. Thus, we chose one of the 4*c* sites, the fractional coordinate of which is (0.5841, 0.25, 0.2251). This compound is described as $Ba_8Si_{16}Ga$.

Table I summarizes the calculated electronic energies for Ba_8Si_{16} doped with a Group 13 element (B, Al, Ga, or In) or a Group 15 element (N, P, As, or Sb). The binding energy of Ba_8Si_{16} is calculated to be −133.696 eV. The total energy after impurity doping is

calculated using the binding energies of the optimized structures as follows: for one P atom replacing one Ba atom at the $Ba^{(1)}$ site, the total energy of $Ba_7P^{(1)}Si_{16}$ + Ba is given by −128.697 − 1.912 = −130.609 eV. Meanwhile, for a P atom replacing a Si atom at the $Si^{(3)}$ site, the total energy of $Ba_8P^{(3)}Si_{15}$ + Si is −131.007 − 5.514 = −136.494 eV. In the same way, the total energy of $Ba_8Si_{16}P$ is calculated to be −135.698 eV. From an energetic point of view, these results imply that replacement of Si with P is most likely to occur in P-doped $BaSi_2$. The same assumption can be applied to doping with other elements, except for B- or O-doped $BaSi_2$—B or O atoms are more likely to occupy an interstitial site.

Fig. 9 shows the total DOSs of impurity-doped $BaSi_2$ near E_F. The DOSs of $Ba_8Si_{16}B$ and $Ba_8Si_{16}O$ are also presented, where their E_F's represent the energy zero. For $BaSi_2$ doped with a Group 13 element, E_F crosses the top of the valence band, E_V, and the resultant doped $BaSi_2$ is p-type. Note that interstitial B gives rise to localized states within the band gap. In $BaSi_2$ doped with a Group 15 element, E_F moves to the bottom of the conduction band, thereby forming an n-type material. The interesting thing from an energetic point of view is that O is most likely to be located at an interstitial site and does not generate defective states within the band gap, whereas other impurities generate states in the band gap. $BaSi_2$ is a Zintl phase compound consisting of an electropositive Ba and an

electronegative Si, where the electropositive Ba donates its electrons to Si, which uses the electrons in the formation of covalent bonds in Si_4 tetrahedra to satisfy valence requirements [56]. It was experimentally confirmed that the Si *p* state is dominant around E_V in $BaSi_2$ [57].

3.3 Ex-situ and in-situ doping

Ex-situ doping by ion implantation has been widely used to control the electrical properties of semiconductors. Generally, ion implantation is accompanied by subsequent annealing to recover implantation damage and activate dopants to produce charge carriers. As for *ex-situ* p-type doping in $BaSi_2$ thin films on Si, Hara *et al*. attempted to use a BF_2 source for ion implantation with a dose of 1.0×10^{12} cm^{-2}–1.0×10^{14} cm^{-2} followed by annealing [58]. They revealed that rapid thermal annealing (RTA) at 700 °C or 800 °C for 30 s could remove implantation damage while suppressing oxidation of $BaSi_2$. Raman spectra indicated that Si sites have been substituted with B after RTA, indicating that B acts as a dopant to achieve p-type $BaSi_2$.

As for *ex-situ* n-type doping, ion implantation of P ions with a dose of 1.0×10^{13} cm^{-2}–1.0×10^{15} cm^{-2} in $BaSi_2$ thin films on Si has been investigated [59]. RTA at 600–800 °C for 30 s was found to be useful to remove implantation damage. However, P atoms segregated and concentrated itself at the surface and $BaSi_2$/Si interface, while the formation of a

metastable trigonal $BaSi_2$ phase was revealed. By reducing the thermal budget to 500 °C for 30 s or 700 °C for 1 s, the suppression of the segregation of P atoms, removal of the implantation damage, and activation of dopants can be simultaneously achieved. As a result, n-type $BaSi_2$ with $n \sim 10^{18}$ cm^{-3} can be obtained with P-doping [60]. Doping of $BaSi_2$ with As ions by ion implantation was also attempted, and the highest possible n was estimated to be less than 2×10^{17} cm^{-3} [61]. Therefore, P-doping is more efficient if one uses ion implantation to obtain n-type $BaSi_2$.

In-situ doping in $BaSi_2$ has been performed by depositing Ba, Si, and impurity atoms on RDE-grown $BaSi_2$ templates [54,62–67]. Impurities were supplied from K-cells. Table 2 summarizes the carrier type and highest carrier concentration achieved so far for impurity-doped $BaSi_2$ by *ex-situ* and *in-situ* methods. In accordance with the calculation results shown in Fig. 9, Group 13 elements give rise to p-type $BaSi_2$ (except for Ga), while Group 15 elements create n-type $BaSi_2$. As for p-type $BaSi_2$, p can only be controlled over a wide range between 10^{16} and 10^{19} cm^{-3} by B doping. In contrast, n can be controlled over a relatively wide range by As, P, or Sb doping.

The diffusion coefficient is a decisive parameter that will affect the steepness of a pn junction. In the case of B, we formed $BaSi_2$ epitaxial layers capped with a 180 nm thick B layer, followed by post-annealing in UHV at different temperatures for various

durations. Fig. 10(a) shows the measured and simulated secondary ion mass spectrometry (SIMS) depth profile of B for a sample annealed at 800 ºC for 1 h. Both lattice and grain boundary (GB) diffusions were taken into consideration to reproduce the experimental profile [68]. The concentration distribution $C(x, t)$ of impurity atoms owing to the lattice diffusion is given by Eq. (1), where $x = 0$ is set at the B/$BaSi_2$ interface and C_0 is the B concentration at $x = 0$, D_l is the lattice diffusion coefficient, and t is the annealing duration. The lattice diffusion length L, which is given by $L = \sqrt{D_l t}$, is also included in Eq. (1).

$$C(x,t) = C_0 \mathrm{erfc}(x / 2\sqrt{D_l t}). \quad (1)$$

To fit the GB diffusion regions, Eq. (2) was employed using type-B kinetic regimes [69],

$$s\delta D_{\mathrm{GB}} = 1.332(D_l / t)^{1/2}\left(-\partial \ln C(x,t) / \partial x^{6/5}\right)^{-5/3}, \quad (2)$$

where s is the segregation factor, δ is the grain boundary width, and D_{GB} is the GB diffusion coefficient. Fig. 10(b) presents the Arrhenius plots for the obtained D_l and sD_{GB}. The diffusion coefficients of impurity atoms in other silicides are also shown for comparison [70]. From Fig. 10(b), we see that the diffusion coefficients of B in $BaSi_2$ are much smaller than others. The reason for this has yet to be clarified.

4. Optical absorption properties

Absorption coefficients of $BaSi_2$ were measured on $BaSi_2$ epitaxial layers formed on a

transparent silicon-on-insulator (SOI) substrate [17]. The substrate was produced by wafer bonding of Si(111) and fused silica wafers at RT, followed by mechanical grinding and polishing by chemical mechanical polishing down to about 0.7 μm thickness. After that, approximately 100 nm thick $BaSi_2$ was epitaxially grown. This is to ensure both high transparency of the substrate and high quality of the $BaSi_2$ films for the optical absorption measurements. The transmission spectra were obtained using a JASCO U-best 570 spectrophotometer. The absorption coefficient of $BaSi_2$ reaches 3×10^4 cm^{-1} at 1.5 eV as shown in Fig. 11(a). This value is almost the same as for the samples formed by vacuum evaporation and by RF sputtering [37,49]. Fig. 11(b) shows the $(\alpha dhv)^{1/2}$ versus hv plot for deriving the indirect optical absorption edge. The straight fit line intersects the horizontal line at 1.34 eV. Thus, the indirect absorption edge with phonon emission is 1.34 eV.

The complex refractive index of $BaSi_2$ $\tilde{n}$ is very important to design the anti-reflection coating and to correctly predict the optical behavior of real devices. It is given by refractive index n_{index} and extinction coefficient κ as $\tilde{n} = n_{\text{index}} + i\kappa$. Their quantities were measured on a 150 nm thick MBE-grown $BaSi_2$ epitaxial film on Si(111) in the range between 300 nm and 1200 nm by spectrophotometry and by spectroscopic ellipsometry [71]. Figure 12 depicts their wavelength dependence. According to ref. 71,

the photocurrent density reaches 41.1 mA/cm^2 under AM1.5 illumination in a 2 μm thick $BaSi_2$ solar cell, suggesting the great potential of $BaSi_2$ for thin-film solar cell applications. Real and imaginary parts of the dielectric constant versus photon energy for $BaSi_2$ was calculated in ref. 9, where the long-wavelength limit of the real part is about 14, hence the refractive index n_{index} is deduced to be about 3.7. This value is close to the long-wavelength limit in Fig. 12. Similar results were obtained for $BaSi_2$ films grown by sputtering [49].

5. Minority-carrier properties

5.1 Minority-carrier lifetime

The recombination of photogenerated excess carriers is of great importance in controlling the solar cell performance. In particular, the bulk minority carrier lifetime τ_b is a fundamental parameter to certify the potential of $BaSi_2$ as an absorber for thin film solar cells. Microwave-detected photoconductivity decay (μ-PCD) has been widely used to investigate the recombination process of excess carriers. Hara *et al*. investigated the recombination process of excess carriers in n-$BaSi_2$ thin films on Si(111) with various film thicknesses by μ-PCD using a 5 ns pulse laser with a wavelength of 349 nm [72]. The measured decay curve was found to be multiexponential and can be divided mainly

into three parts based on the decay rate, as shown in Fig. 13(a). Because of the indirect nature of $BaSi_2$, intrinsic radiative recombination is not the determining process. The initial rapid decay at higher carrier densities was assigned to Auger recombination. Then, over time, the decay curve is controlled by Shockley-Read-Hall (SRH) recombination with and without carrier trapping effects. To obtain τ_b in n-$BaSi_2$, post-growth annealing was carried out at 800 °C for 30 s [73]. This annealing process causes a drastic increase in excess carrier lifetime and allows the investigation of the recombination process at low injection levels. We attribute this increase in the minority-carrier lifetime to an oxidation of the sample surface, which was shown with excellent repeatability to increase the minority-carrier lifetime as described in section 5.3. It should be noted that the excess carrier density should be much lower than the majority carrier (electron) density in n-$BaSi_2$ ($n \sim 5 \times 10^{15}$ cm^{-3}). Fig. 13(b) shows the inverse of the apparent lifetime measured at a low injection level as a function of the inverse of the film thickness [74]. From this curve, τ_b was determined to be 14 μs in n-$BaSi_2$. The corresponding minority carrier diffusion length is considered to be much longer than calculated given the absorber thickness. In addition, the sum of the surface and interface recombination velocities was found to be 8.3 cm/s, which is extremely low and confirms that $BaSi_2$ is promising for solar cell applications.

5.2 Minority-carrier diffusion length

Along with the minority-carrier lifetime, minority-carrier diffusion length is a measure by which to characterize absorber materials. To achieve higher efficiencies in a solar cell, a longer minority-carrier diffusion length is essential [75]. We evaluated those for $BaSi_2$ on Si(111), L_{111}, and for $BaSi_2$ on Si(001), L_{001}, with the electron-beam-induced current (EBIC) technique. Three hundred to four hundred nanometer thick n-$BaSi_2$ epitaxial layers were grown by MBE on n-Si(111) (resistivity $\rho = 0.1$ Ω·cm) and n-Si(001) ($\rho = 0.1$ Ω·cm). The backside ohmic contact was deposited by vacuum evaporation. Scanning electron microscopy (JEOL JSM7600F) was employed for the EBIC measurements. An elastic tiny tungsten (W) probe [76] was gently placed on the $BaSi_2$ surface so as not to cause surface damage; it forms a Schottky contact with n-$BaSi_2$ on n-Si(001) and determined a short minority-carrier diffusion length [19]. Instead of the W probe, a Schottky contact with Al wire was used for n-$BaSi_2$ on n-Si(111) [18]. The acceleration voltage of the electron beam was set at 5 kV to avoid penetration of the electron beam into the Si substrate. Thus, the effect of carriers generated in the Si substrate can be neglected.

Figs. 14(a) and 14(a') show secondary electron (SE) and EBIC images, respectively, of $BaSi_2$ on Si(111), and Figs. 14(b) and 14(b') show those of $BaSi_2$ on

Si(001). In the EBIC method, the carriers generated within a diffusion length of n-type $BaSi_2$ are collected by the electric field under the Schottky contact and sensed as a current in the external circuit. The brighter regions indicate the higher collection of electron-beam-induced carriers in $BaSi_2$. Fig. 14(c) shows the plots of EBIC line-scan data along the lines AA' and BB' in Figs. 14(a') and 14(b'), respectively. The EBIC profiles show a clear exponential dependence on the distance from the metal contacts. The contribution of carriers generated within the n-Si substrate to the measured EBIC signals can be excluded as described above. In this work, L_{001} was estimated to be approximately 1.5 μm in $BaSi_2$ on Si(001), assuming that the EBIC profile varies as $\exp(-x/L)$, where x is the distance from the metal edge along the line and L is the diffusion length of holes for $BaSi_2$. In contrast, L_{111} was deduced to be approximately 10 μm in $BaSi_2$ on Si(111). We performed the same experiments more than 10 times, and similar results were obtained. Figs. 14(d) and 14(d') present the plan-view bright-field TEM images of these samples. The incident electron beam was almost parallel to the $BaSi_2$[100] zone axis, but it was slightly tilted for the GBs to be seen clearly. At a first glance, sharp GBs are present in $BaSi_2$ on Si(111), while roundish ones are found in $BaSi_2$ on Si(001); dark spots corresponding to defects are located along the GBs. Besides, the grain size of $BaSi_2$ on Si(111) is much smaller than that on Si(001), which differs from our predictions that arise

from $L_{111} > L_{001}$. These results show that L_{111} is much larger than L_{001}, even though the domain size of $BaSi_2$ is much smaller in $BaSi_2$ on Si(111) than in $BaSi_2$ on Si(001). The difference in the minority-carrier diffusion length is related to the difference in the potential variations across the GBs as described in Section 6.1. On the basis of these results, we conclude that a Si(111) surface is more suitable for $BaSi_2$ growth than a Si(001) surface from the viewpoint of minority carrier diffusion length, which is important in solar cell applications.

The minority-carrier properties of doped $BaSi_2$ is also important. We employed 0.5 μm thick B-doped p-$BaSi_2$ epitaxial films on Si(111) for this purpose. Fig. 15 shows the p dependence of minority-carrier lifetime measured by μ-PCD and minority-carrier diffusion length evaluated by EBIC using the W probe. The acceleration voltage of the electron beam was set at 5 kV. The minority-carrier lifetime increases from 0.07 μs to 2 μs as the p decreases from 3.9×10^{18} cm^{-3} to 1.4×10^{16} cm^{-3}. The minority-carrier diffusion length also increases with decreasing the p, and exceeds 1 μm at $p = 1 \times 10^{17}$ cm^{-3}. Evaluation of minority-carrier properties in impurity-doped n-$BaSi_2$ is also required.

5.3 Surface passivation

For device applications, surface passivation is very important for materials like $BaSi_2$,

which possess large α, because short-wavelength light is absorbed in the region close to the surface. Therefore, a defective surface deteriorates solar cell performance. μ-PCD measurements showed that τ reaches approximately 10 μs with excellent repeatability for n-$BaSi_2$ by means of capping the $BaSi_2$ surface with the native oxide or a few nanometers thick a-Si layer [77]. Note that we did not incorporate hydrogen atoms in the a-Si layers because we did not have such equipment. We also need to confirm that such surface passivation layers do not deteriorate the carrier transport across the native-oxide/$BaSi_2$ or a-Si/$BaSi_2$ interface. Hard X-ray photoelectron spectroscopy (HAXPES) is a powerful tool to directly probe the VB DOS of $BaSi_2$ under the capping layers. This is because the analysis-depth of HAXPES is much deeper than that of conventional X-ray photoelectron spectroscopy and ultraviolet photoelectron spectroscopy. An extremely brilliant X-ray provided from a third generation synchrotron source can sufficiently compensate for the diminished cross section and has enabled us to perform HAXPES measurements with high-energy resolution [78]. There have been several reports utilizing this large probing depth on the measurement of VB spectra of buried layers such as CdS/Cu_2ZnSnS_4 (CZTS), and AlO_x/Si heterostructures, and Bi_2Se_3 surface [79-81]. For example, in ref. 78, CdS/CZTS heterostructures formed on Mo-coated glass, where the CdS layer thickness was varied (0, 5, and 100 nm), was examined by changing the effective inelastic mean

free path, which was controlled by the take-off-angle (TOA) of photoelectrons in HAXPES. Consequently, they succeeded in measuring the VB spectra of CdS and CZTS, separately, and obtained a VB offset (VBO) at the CdS/CZTS interface of 0.0 ± 0.1 eV in a real device structure. To examine the VBO, native-oxide/n-$BaSi_2$(600 nm)/Si(111) and a-Si(5 nm)/n-$BaSi_2$(730 nm)/Si(111) samples were prepared by MBE.

Figs. 16(a) and 16(b) show the bright-field TEM cross sections of the samples [82]. We see that a 5 nm thick a-Si layer is uniformly formed on the n-$BaSi_2$ surface as expected and that the a-Si/$BaSi_2$ interface has a sharp interface. The fact that the a-Si layer thickness is almost the same as the deposited thickness monitored by a quartz crystal microbalance system indicates that the oxidation of the a-Si terminates near the surface. An approximately 8 nm thick native oxide layer is formed on $BaSi_2$.

Fig. 17(a) shows the Ba $3d_{5/2}$ core-level spectra of a-Si/$BaSi_2$, taken at TOA = 15°, 30°, and 90° [82]. Fig. 17(b) is the spectra of Fig. 17(a) normalized to the peak located at −780.6 eV. In Fig. 17(b), we see only one peak located at −780.6 eV at TOA = 30° and 90°. We attribute this peak to the $BaSi_2$ layer. In contrast, the spectrum measured at TOA = 15° was well reproduced with a peak-fitting analysis by adding another Gaussian curve located at −781.1 eV, which is probably caused by slight oxidation of $BaSi_2$, as described below. Fig. 17(c) shows the Ba $3d_{5/2}$ core-level spectra of native-

oxide/$BaSi_2$, taken at TOA = 15°, 30°, and 90°. At TOA = 30° and 90°, each spectrum was well reproduced by two Gaussian curves located at −780.6 eV and −781.7 eV. At TOA = 15°, however, one Gaussian curve located at −781.7 eV was enough to reconstruct the measured spectrum. The peak located at −781.7 eV became stronger as TOA decreased. We therefore attribute this peak to the surface native oxide because the contribution of this peak appeared dominant in the surface-sensitive measurement (TOA = 15°). Hence, it is clear that the a-Si layer suppresses the oxidation of the $BaSi_2$ layer in the a-Si/$BaSi_2$ sample. Furthermore, the peak positions did not shift regardless of TOA (i.e., analysis depth) in Figs. 17(a) and 17(b), meaning that band bending did not occur or it was negligibly small in $BaSi_2$ near the a-Si/$BaSi_2$ interface.

Fig. 17(a') shows the Si 2*s* core-level spectra for a-Si/$BaSi_2$, taken at TOA = 15°, 30°, and 90° [82]. Fig. 17(b') is the spectra of Fig. 17(a') normalized to the peak located around −151 eV. The ratio of the peak intensity around −155 eV to that around −151 eV increased as the TOA decreased, indicating that the peak around −155 eV is caused by surface oxides. Note that the peak position located around −151 eV was shifted by approximately 0.2 eV as TOA was decreased from 90° to 15°. As discussed before, band bending did not occur in $BaSi_2$ near the a-Si/$BaSi_2$ interface. Therefore, we attribute this peak shift to band bending in the a-Si layer. As seen in Fig. 17(c'), the peak intensities of

the oxides became stronger for the native-oxide/$BaSi_2$ sample as TOA decreased; the peak located around −151 eV almost disappeared at TOA = 15°. Considering the Si 2*s* core-level spectra as well as the Ba $3d_{5/2}$ core-level spectra, it is therefore reasonable to assume that a-Si suppresses surface oxidation by capping the surface with a-Si [82,83].

Fig. 18 presents the obtained VB alignment of $BaSi_2$ with respect to the top of the VBs of native oxide, $E_{V,oxide}$ and a-Si, $E_{V,a\text{-}Si}$. The result means that the transport of holes is not blocked at the a-Si/$BaSi_2$ interface, but is blocked at the native-oxide/$BaSi_2$ interface instead owing to a large barrier height of about 3.9 eV. To confirm hole transport across the interface, we compared the photoresponse spectra of a 500 nm thick n-$BaSi_2$ layer capped with either a 3 nm thick a-Si or native-oxide layer. Two hundred nanometer thick indium tin oxide (ITO) surface electrodes with a diameter of 1 mm and Al rear electrodes were fabricated by sputtering. Photoresponse and reflectance (*R*) spectra were evaluated at RT via a lock-in technique using a xenon lamp with a 25 cm focal length single monochromator (Bunko Keiki SM-1700A and RU-60N).

Figs. 19(a) and 19(b) present the photoresponse and reflectance spectra of these samples [84]. The bias voltages were applied so that the photogenerated holes in n-$BaSi_2$ were transferred to the surface electrode (ITO) across the a-Si/n-$BaSi_2$ or native-oxide/n-$BaSi_2$ interface. The photoresponsivity of $BaSi_2$ was drastically improved by

approximately five times with the a-Si capping layer compared to without the capping layer. This is ascribed to the difference in the hole transport properties between the a-Si/n-$BaSi_2$ and native-oxide/n-$BaSi_2$ interfaces. Note that the reflectance of the two samples is almost the same, therefore the number of photogenerated carriers should be almost the same. The results presented in Fig. 19 are consistent with the band lineups shown in Fig. 18, obtained by HAXPES.

6. Properties of grain boundaries

The minority-carrier diffusion length, a key parameter determining the performance of solar cells, was found to be approximately 10 μm in the n-$BaSi_2$ epitaxial film on Si(111) by MBE; this was determined via an EBIC measurement, as shown in Fig. 14(c) [18]. This value is much larger than the grain size of $BaSi_2$ (~0.2 μm), implying that the GBs do not work as defect centers for minority carriers (holes) in n-$BaSi_2$. Kelvin probe force microscopy (KFM) is considered one of the most powerful methods for evaluating potential variations in the GB characteristics. For polycrystalline Si and compound semiconductors, the GBs characteristics have been discussed in detail in terms of GB band lineup and barrier height using KFM [85–88]. In this study, we analyzed the potential variations and barrier heights around GBs in $BaSi_2$ epitaxial films both on

Si(111) and Si(001) substrates using KFM in air.

Figs. 20(a) and 20(b) show the 5 × 5 μm^2 AFM topographic and KFM electrostatic potential (ϕ) images, respectively, of n-$BaSi_2$ epitaxial layers on Si(111) by MBE; the cross sectional profiles along the white lines in the same areas are also shown [23]. The positions of the colored lines correspond to those of the GBs in the cross sectional profiles in Figs. 20(a) and 20(b). The electrostatic potentials at the GBs are higher than those in the grains. Since the energy band lineup is defined for negatively loaded electrons, the potential corresponds to the inverse of the work function divided by the elemental charge. This result means that band bending occurs downwards at the GBs, as shown in Fig. 20(c). The histogram of the barrier height is shown in Fig. 20(d). The barrier height for holes is positive and its absolute value ranges from 10 to 60 meV and the average is approximately 30 meV. This value is almost the same as the thermal energy of 26 meV at RT (25 °C). The concave band structure at the GBs in the $BaSi_2$ on Si(111) are supposed to lead to repulsion of photogenerated holes (minority carriers) from the GBs, reducing the charge carrier recombination at the GBs. Therefore the GBs do not work as recombination centers for the minority carriers in n-$BaSi_2$. This explains the long minority carrier diffusion length, which reaches 10 μm even for multi-domain epitaxial $BaSi_2$ films on Si(111).

Figs. 21(a) and 21(b) show the 5 × 5 μm^2 AFM topographic and KFM electrostatic potential images, respectively, measured for n-$BaSi_2$ epitaxial layers by MBE on Si(001) [23]. Their cross sectional profiles along the white lines in the same area are also shown. In the case of $BaSi_2$ grown on Si(001), one type of variant was dominantly grown. We see that the $BaSi_2$ grains extend in the Si[110] direction in Fig. 21(a). Therefore, we investigated the electrostatic potentials along the line AA', parallel to Si[110], and also along the line BB', parallel to Si[1-10] because those GBs are composed of different planes. The GBs have a lower electrostatic potential than the inner parts of the grains, meaning that band bending occurs upwards at the GBs, as shown in Fig. 21(c). The difference in the band bending at the GBs between n-$BaSi_2$/Si(111) and n-$BaSi_2$/Si(001) is attributed to the difference in the $BaSi_2$ planes, which consist of GBs. GBs along line AA' are composed of $BaSi_2$(001) planes. For GBs along line BB', we do not yet have enough data to currently discuss this. We should note here that impurity contaminations can also cause potential variations around GBs. Impurity segregation to GBs have been extensively studied in poly crystalline Si [89–91]. Tsurekawa *et al*. confirmed that the GBs in Cu- and Fe-contaminated *p*-type Si cause a significant increase in the barrier height compared to non-contaminated Si [92]. We cannot exclude this possibility to explain the potential variations at the GBs of $BaSi_2$ films. There have so far

been no reports on the segregation of impurities toward GBs in $BaSi_2$. Thus, detailed studies of impurity segregation in $BaSi_2$ will be required in the near future.

We also investigated the potential distribution of GBs in n-$BaSi_2$ formed by MBE on multicrystalline Si (mc-Si) [93]. KFM measurements show that the potentials are not significantly disordered in the grown $BaSi_2$, even around the GBs of mc-Si. The potentials are higher at the GBs of $BaSi_2$ around Si GBs that are formed by grains with a Si(111) face and with faces that deviate slightly from Si(111). Thus, downward band bending occurs at these $BaSi_2$ GBs. Minority carriers (holes) undergo a repelling force near the GBs, which may suppress recombination, as in the case of n-$BaSi_2$ epitaxial films on a single crystal Si(111) substrate. The barrier height for hole transport across the GBs varies in the range of 10 to 55 meV. The potentials are also higher at the $BaSi_2$ GBs grown around Si GBs composed of grains with Si(001) and Si(111) faces. The barrier height for hole transport ranges from 5 to 55 meV. These results indicate that $BaSi_2$ GBs formed on (111)-dominant Si surfaces do not have a negative influence on the minority-carrier properties, and thus $BaSi_2$ formed on underlayers, such as (111)-oriented Si or Ge and on (111)-oriented mc-Si, can be used as a solar cell active layer. We also discussed the potential variation across the GBs in impurity-doped n-type or p-type $BaSi_2$ epitaxial films [94].

In ref. 95, the atomic arrangements around the GBs in an n-$BaSi_2$ epitaxial film on Si(111) by MBE were observed by TEM, and the most stable atomic configuration was determined by first-principles calculations based on DFT to provide four possible interface models. Each model is consistent with TEM observations and is distinguished by the relationship between the Si tetrahedron arrays in the two domains adjacent across the interface. One of the four interface models whose relationship between first-neighboring Si tetrahedra across the interface was the same as that in the bulk was particularly stable, and showed no significant differences in the partial DOSs and band gap between the bulk and GB regions. We now know the positions of Ba and Si atoms in the most stable interface structure, hence, the results should be applicable to further studies such as the effects of impurities around GBs upon the electronic properties of $BaSi_2$.

7. $BaSi_2$/Si hererojunction solar cells

A pn homojunction diode is the most straightforward structure of a solar cell. In ref. 96, the spectral response of $BaSi_2$ p^+n abrupt homojunction diodes is discussed using experimentally obtained absorption coefficients, minority-carrier diffusion lengths, and minority-carrier lifetimes, where $\eta > 25\%$ is expected for 2 μm thick $BaSi_2$ homojunction

solar cells under ideal conditions. Here, however, we choose to begin with a p-$BaSi_2$/n-Si heterojunction structure [65]. Fig. 22(a) shows the expected band alignment of a p-$BaSi_2$/n-Si junction diode when p is 2.2×10^{18} cm^{-3} for p-$BaSi_2$ and n is 2.0×10^{15} cm^{-3} for n-Si. Hence, the depletion region stretches into the n-Si region. The electron affinities of $BaSi_2$ and Si are $q\chi_{BaSi2}$ = 3.2 eV [97] and $q\chi_{Si}$ = 4.05 eV, respectively, and their bandgaps are $E_{g,BaSi2}$ = 1.3 eV and $E_{g,Si}$ = 1.1 eV. There is a conduction band offset ΔE_C = 4.05 − 3.2 ≈ 0.9 eV and a valence band offset ΔE_V = (4.05 + 1.1) − (3.2 + 1.3) ≈ 0.7 eV at the heterointerface. The band offsets ΔE_C and ΔE_V in Fig. 22(a) promote the separation of photogenerated electrons and holes in p-$BaSi_2$, as well as those in n-Si, which is how it operates as a solar cell. Therefore, we anticipate that $BaSi_2$ will be useful as a hole selective contact for c-Si solar cells.

On an n-Si(111) substrate, we formed B-doped p-$BaSi_2$ epitaxial layers with various layer thicknesses $d_{p\text{-}BaSi_2}$ ranging from 10 nm to 50 nm by MBE, followed by a 3–4 nm thick a-Si capping layer. We set p in the p-$BaSi_2$ sample to 2×10^{18} cm^{-3}. Finally, 1 mm diameter and 70 nm thick ITO electrodes were sputtered on the front surface, and Al electrodes were deposited on the backside of the n-Si substrate. The a-Si capping layer is necessary to prevent surface oxidation of the p-$BaSi_2$ and to ensure efficient hole transport to the ITO [82]. The a-Si layer thickness was determined to suppress the light

absorption in the a-Si layer [98]. Fig. 22(b) shows a bright-field cross-sectional TEM image for $d_{\text{p-BaSi}_2}$ = 20 nm. Both the a-Si/$BaSi_2$ and $BaSi_2$/n-Si interfaces are very smooth and there are no B precipitations observed in the $BaSi_2$ layer.

Fig. 23(a) shows current–density versus voltage (*J*–*V*) curves under AM1.5 illumination [99]. All the samples performed as solar cells. This result clearly demonstrates that the p-$BaSi_2$/n-Si heterointerface does not hinder the transport of photogenerated electrons in p-$BaSi_2$ to the n-Si side, and photogenerated holes in n-Si migrate to the p-$BaSi_2$ side as expected in Fig. 22(a). The short-circuit current density J_{SC} reaches a maximum of 36.2 mA/cm^2, and the open-circuit voltage V_{OC} increases with $d_{\text{p-BaSi}_2}$ and reaches a maximum of 0.47 V at $d_{\text{p-BaSi}_2}$ = 20 nm. Fig. 23(b) shows spectra for the internal quantum efficiency (*IQE*), external quantum efficiency (*EQE*), and reflectance (*R*) at $d_{\text{p–BaSi}_2}$ = 20 nm. The *EQE* is resolved into the contribution of $BaSi_2$, *EQE*($BaSi_2$), and that of Si, *EQE*(Si), using absorption coefficients of $BaSi_2$. The *EQE*($BaSi_2$) is much smaller than the *EQE*(Si), hence, we can say that the p-$BaSi_2$ does not function as an absorber layer but a window layer in the present device.

For detailed discussions, parameters including the conversion efficiency η and fill factor (*FF*) are summarized in Fig. 24. η reaches a maximum of 9.9%, the highest value ever reported for semiconducting silicides [84]. J_{SC} increases until $d_{\text{p-BaSi}_2}$

reaches 20 nm, and then decreases with $d_{\text{p-BaSi}_2}$. This means that the transport of photogenerated electrons in the p-$BaSi_2$ to the n-Si was disturbed when $d_{\text{p-BaSi}_2}$ becomes large. V_{OC} almost saturates at $d_{\text{p-BaSi}_2}$ = 20 nm and above, while J_{SC} decreases. This result suggests that the reverse-bias saturation current density J_0 decreases with $d_{\text{p-BaSi}_2}$, because in an ideal case, V_{OC} is given by:

$$V_{\text{OC}} \approx \frac{k_{\text{B}}T}{q} \exp\left(\frac{J_{\text{SC}}}{J_0} \right). \qquad (2)$$

In the present device, p was set to a relatively large value of 2×10^{18} cm^{-3}. So it becomes difficult for the photogenerated minority carriers (electrons) in p-$BaSi_2$ to diffuse to the n-Si side before recombination for large $d_{\text{p-BaSi}_2}$. This might be the reason why the J_{SC} decreases as $d_{\text{p-BaSi}_2}$ exceeds 20 nm.

Regarding the stability of these solar cells, the η was measured for as many electrodes as possible in an area of 1×1 cm^2 on the p-$BaSi_2$(20 nm)/n-Si solar cells, capped with a 2 nm or 3 nm thick a-Si. p was set to approximately 2×10^{18} cm^{-3}. Solar cell samples were stored with other samples in a simple desiccator with a reduced-pressure atmosphere (~76 Torr) for various durations up to 226 days since their first fabrication in January of 2016. Every time we measured η of the solar cells, we let air into the desiccator and took the samples out. Other than that, the desiccator was frequently exposed to air to put in or take out other samples in a day. The η was plotted against time

in Fig. 25 [100], demonstrating that the η does not degrade. During such a long storage period, O are considered to incorporate into the $BaSi_2$ layers. First-principles calculation reveal that the O atoms are supposed to be positioned at the interstitial sites called the 4*c* sites rather than substitutional sites, differently from Group 13 or 15 elements, and do not create localized states within the band gap [101]. This is perhaps one of the reasons why O, which may interact strongly with $BaSi_2$, seems to have no detrimental effect on the performance of solar cells.

Note that we will be able to convert the present p-$BaSi_2$/n-Si heterojunction structure into a $BaSi_2$ pn homojunction diode by forming an n-$BaSi_2$ layer on a lightly-doped relatively thick p-$BaSi_2$ absorber-layer grown on a Si substrate with small ρ, and further to a $BaSi_2$-pn/Si-pn tandem structure. Replacing half the $Ba^{(1)}$ sites with isoelectric Sr expands the band gap of $BaSi_2$ by 0.1 eV [102–105]. A broadening of the band gap by substituting Ba with Sr [106] and by substituting Si with C is theoretically expected [107]. It is safe to state that there is still plenty of room for improvement in η as well as in $BaSi_2$ device structures.

8. Summary

In this article, we review the potential application of $BaSi_2$ as a solar cell material, from

the fundamental properties of $BaSi_2$ to the latest results on $BaSi_2$ solar cells in which η approaches 10%. $BaSi_2$ has a high absorption coefficient comparable to CIGS, a long minority-carrier lifetime, and a band gap close to 1.4 eV. Further, $BaSi_2$, composed of safe, stable, and earth-abundant elements, is compatible with crystalline silicon solar cells because $BaSi_2$ can be grown epitaxially on Si(001) and Si(111) surfaces. One of the striking features of this material is that both its high absorption coefficient and large minority-carrier lifetime can be used. This arises from the energy band structure of $BaSi_2$. Present commercialized solar cell materials like Si, CdTe, and CIGS do not possess these material properties. $BaSi_2$ thus has the potential to be the market leader in the future. Towards this goal, our top priority is to achieve the solar cell operation of a $BaSi_2$ homojunction diode. There is no obvious barrier to it at the moment. However, we have only limited information on the following material properties that may affect the solar cell performance: (1) bulk defects such as dislocations and their influence on minority-carrier properties and transport properties of carriers, (2) surface passivation by conventional hydrogenated a-Si layers in place of not-hydrogenerated ones used thus far, (3) minority-carrier properties of impurity-doped $BaSi_2$, especially, impurity-doped n-$BaSi_2$, and (4) scattering mechanisms that limit the mobility of carriers. Development of low-temperature gas-phase growth technique is also desired. We therefore hope that many

researchers will be interested in using this material.

Acknowledgements

The author acknowledges Dr. K. O. Hara of the University of Yamanashi, Dr. T. Sekiguchi of the National Institute for Materials Science (NIMS), Dr. K. Watanabe of Osaka University, and Dr. C. T. Trinh of Helmholz Zentrum Berlin for their help, discussions, and encouragements to pursue this work. Special thanks are to Dr. K. Toko, Dr. W. Du, Dr. M. Ajmal Khan, and present and past students of the University of Tsukuba and Nagoya University for their experiments and fruitful discussions. HAXPES measurements were conducted at Synchrotron X-ray station of BL15XU, at SPring-8, with the help of Professor A. Kimura of Hiroshima University and Dr. S. Ueda of NIMS, under the program of "Nanotechnology platform" (Proposal Nos. 2014A4902, 2015A4907, and 2015B4906) of the Ministry of Education, Culture, Sports, Science and Technology (MEXT), Japan. This work was financially supported in part by the Core Research for Evolutionary Science and Technology (CREST) of the Japan Science and Technology Agency (JST) and by a Grant-in-Aid for Scientific Research (A) (No. 15H02237) from the JSPS.

[1] ITRPV Seventh Edition 2016 Version 2, http://www.itrpv.net/Reports/

[2] NEDO News Release, http://www.nedo.go.jp/english/news/AA5en_100109.html

[3] W. Shockley and H. J. Queisser, J. Appl. Phys. **32**, 519 (1961).

[4] H. K. Janzon, H. Schafer, and A. Weiss, Z. Anorg. Allg. Chem. **372**, 87 (1970).

[5] J. Evers, G. Oehlinger, and A. Weiss, Angew. Chem. Int. Ed. Engl. **16**, 659 (1977).

[6] M. Imai and T. Hirano, Phys. Rev. B **58**, 11922 (1998).

[7] Y. Imai, A. Watanabe, and M. Mukaida, J. Alloy and Comp. **358**, 257 (2003).

[8] L. I. Ivanenko, V. L. Shaposhnikov, A. B. Filonov, A. V. Krivosheeva, V. E. Borisenko,

D. B. Migas, K. Miglio, G. Behr, and J. Schumann, Thin Solid Films **461**, 141 (2004).

[9] D. B. Migas, V. L. Shaposhnikov, and V. E. Borisenko, Phys. Status Solidi

B **244**, 2611 (2007).

[10] M. Kumar, N. Umezawa, and M. Imai, Appl. Phys. Express **7**, 071203 (2014).

[11] M. Kumar, N. Umezawa, and M. Imai, J. Appl. Phys. **115**, 203718 (2014).

[12] G. Kresse and D. Joubert, Phys. Rev. B **59**, 1758 (1999).

[13] P. E. Blöchl, Phys. Rev. B **50**, 17953 (1994).

[14] J. Perdew and Y. Wang, Phys. Rev. B **45**, 13244 (1992).

[15] H. J. Monkhorst and J. D. Pack, Phys. Rev. B **13**, 5188 (1976).

[16] K. Morita, Y. Inomata, and T. Suemasu, Thin Solid Films **508**, 363 (2006).

[17] K. Toh, T. Saito, and T. Suemasu, Jpn. J. Appl. Phys. **50**, 068001 (2011).

[18] M. Baba, K. Toh, K. Toko, N. Saito, N. Yoshizawa, K. Jiptner, T. Sakiguchi, K. O. Hara, N. Usami, and T. Suemasu, J. Cryst. Growth **348**, 75 (2012).

[19] M. Baba, K. Watanabe, K. O. Hara, K. Toko, T. Sekiguchi, N. Usami, and T. Suemasu, Jpn. J. Appl. Phys. **53**, 078004 (2014).

[20] K. O. Hara, N. Usami, K. Toh, M. Baba, T. Toko, and T. Suemasu, J. Appl. Phys. **112**, 083108 (2012).

[21] K. O. Hara, N. Usami, K. Nakamura, R. Takabe, M. Baba, K. Toko, and T. Suemasu, Appl. Phys. Express **6**, 112302 (2013).

[22] R. Takabe, K. O. Hara, M. Baba, W. Du, N. Shimada, K. Toko, N. Usami, and T. Suemasu, J. Appl. Phys. **115**, 193510 (2014).

[23] M. Baba, S. Tsurekawa, K. Watanabe, W. Du, K. Toko, K. O. Hara, N. Usami, T. Sekiguchi, and T. Suemasu, Appl. Phys. Lett. **103**, 142113 (2013).

[24] R. A. Mackee, F. J. Walker, J. R. Conner, and R. Raj, Appl. Phys. Lett. **63**, 2818 (1993).

[25] H. H. Weitering, Sur. Sci. **355**, L271 (1996).

[26] Y. Inomata, T. Nakamura, T. Suemasu, and F. Hasegawa, Jpn. J. Appl. Phys. **43**, 4155 (2004).

[27] Y. Inomata, T. Nakamura, T. Suemasu, and F. Hasegawa, Jpn. J. Appl. Phys. **43**, L478 (2004).

[28] K. Toh, K. O. Hara, N. Usami, N. Saito, N. Yoshizawa, K. Toko, and T. Suemasu, J. Cryst. Growth **345**, 16 (2012).

[29] R. Takabe, K. Nakamura, M. Baba, W. Du, M. Ajmal Khan, K. Toko, M. Sasase, N. Usami, and T. Sueamsu, Jpn. J. Appl. Phys. **53**, 04ER04 (2014).

[30] T. Suemasu, M. Sasase, Y. Ichikawa, M. Kobayashi, and D. Tsukada, J. Cryst. Growth **310**, 1250 (2008).

[31] K. Toh, K. O. Hara, N. Usami, N. Saito, N. Yoshizawa, K. Toko, and T. Suemasu, Jpn. J. Appl. Phys. **51**, 095501 (2012).

[32] K. O. Hara, N. Usami, K. Toh, K. Toko, and T. Suemasu, Jpn. J. Appl. Phys. **51**, 10NB06 (2012).

[33] M. Baba, K. Nakamura, W. Du, M. Ajmal Khan, S. Koike, K. Toko, N. Usami, N. Saito, N. Yoshizawa, and T. Sueamsu, Jpn. J. Appl. Phys. **51**, 098003 (2012).

[34] Y. Nakagawa, K. O. Hara, T. Suemasu, and N. Usami, Jpn. J. Appl. Phys. **54**, 08KC03 (2015).

[35] M. Somer, Z. Allg. Chem. **626**, 2478 (2000).

[36] N. Murakoso, H. Yamaguchi, M. Iinuma, T. Suemasu, and Y. Terai, Asia-Pacific

Conference on Semiconducting Silicides and Related Materials, 17-P31, Fukuoka, Japan, July 17, 2016.

[37] K. O. Hara, Y. Nakagawa, T. Suemasu, and N. Usami, Jpn. J. Appl. Phys. **54**, 07JE02 (2015).

[38] Y. Nakagawa, K. O. Hara, T. Suemasu, and N. Usami, Energy Procedia **141**, 23 (2016).

[39] K. O. Hara, J. Yamanaka, K. Arimoto, K. Nakagawa, T. Suemasu, and N. Usami, Thin Solid Films **595**, 68 (2015).

[40] M. Imai, Jpn. J. Appl. Phys. **50**, 101801 (2011).

[41] T. Suhara, K. O. Hara, Y. Nakagawa, T. Suemasu, and N. Usami, Spring Meeting of the Japan Society of Applied Physics, 14a-A25-9, Hiratsuka, Japan, March 14, 2015.

[42] C. T. Trinh, Y. Nakagawa, K. O. Hara, R. Takabe, T. Suemasu, and N. Usami, Asia-Pacific Conference on Semiconducting Silicides and Related Materials, 17-PM-V-4, Fukuoka, Japan, July 17, 2016.

[43] Y. Nakagawa, C. T. Trinh, K. O. Hara, Y. Kurokawa, T. Suemasu, and N. Usami, Asia-Pacific Conference on Semiconducting Silicides and Related Materials, 17-PM-V-5, Fukuoka, Japan, July 17, 2016.

[44] M. M. Alkaisi and M. J. Thompson, Solar Cells **1**, 91 (1979).

[45] T. D. Moustakas and R. Friedman, Appl. Phys. Lett. **40** , 515 (1982).

[46] J. S. Seol, S. Y. Lee, J. C. Lee, H. D. Nam, and K. H. Kim, Sol. Energy Mater. and Sol. Cells **75**, 155 (2003).

[47] Z. Yang, Z. Hao, Q. Xiea, Physics Procedia **11**, 118 (2011).

[48] T. Yoneyama, A. Okada, M. Suzuno, T. Shibutami, K. Matsumaru, N. Saito, N. Yoshizawa, K. Toko, and T. Suemasu, Thin Solid Films **534**, 116 (2013).

[49] N. A. A. Latiff, T. Yoneyama, T. Shibutami, K. Matsumaru, K. Toko, and T. Suemasu, Phys. Status Solidi C **10**, 1759 (2013).

[50] W. Du, M. Baba, K. Toko, K. O. Hara, K. Watanabe, T. Sekiguchi, N. Usami, and T. Suemasu, J. Appl. Phys. **115**, 223701 (2014).

[51] K. O. Hara, J. Yamanaka, K. Arimoto, K. Nakagawa, T. Suemasu, and N. Usami, Thin Solid Films **595**, 68 (2015).

[52] K. O. Hara, Cham Thi Trinh, K. Arimoto, J. Yamanaka, K. Nakagawa, Y. Kurokawa, T. Suemasu, and N. Usami, J. Appl. Phys. **120**, 045103 (2016).

[53] M. Kumar, N. Umezawa, and M. Imai, Spring Meeting of the Japan Society of Applied Physic, 21a-S223-2, Tokyo, Japan, March 21, 2016.

[54] M. Kobayashi, Y. Matsumoto, Y. Ichikawa, D. Tsukada, and T. Suemasu, Appl. Phys. Express **1**, 051403 (2008).

[55] Y. Imai and A. Watanabe, Intermetallics **15**, 1291 (2007).

[56] S. M. Kauzlarich, Chemistry, Structure, and Bonding of Zintl Phases and Ions, 1st ed. (Wiley-VCH, 1996).

[57] M. Baba, K. Ito, W. Du, T. Sanai, K. Okamoto, K. Toko, S. Ueda, Y. Imai, A. Kimura, and T. Suemasu, J. Appl. Phys. **114**, 123702 (2013).

[58] K. O. Hara, N. Usami, Y. Hoshi, Y. Shiraki, M. Suzuno, K. Toko, and T. Suemasu, Jpn. J. Appl. Phys. **50**, 121202 (2011).

[59] K. O. Hara, Y. Hoshi, N. Usami, Y. Shiraki, K. Nakamura, K. Toko, and T. Suemasu, Thin Solid Films **534**, 470 (2013).

[60] K. O. Hara, Y. Hoshi, N. Usami, Y. Shiraki, K. Nakamura, K. Toko, T. Suemasu, Thin Solid Films **557**, 90 (2014).

[61] K. O. Hara, N. Usami, M. Baba, K. Toko, T. Suemasu, Thin Solid Films **567**, 105 (2014).

[62] M. Ajmal Khan, T. Saito, K. Nakamura, M. Baba, W. Du, K. Toh, K. Toko, and T. Suemasu, Thin Solid Films **522** , 95 (2012).

[63] M. Ajmal Khan, K. O. Hara, W. Du, M. Baba, K. Nakamura, M. Suzuno, K. Toko, N. Usami, and T. Suemasu, Appl. Phys. Lett. **102**, 112107 (2013).

[64] M. Ajmal Khan, K. Nakamura, W. Du, K. Toko, N. Usami, and T. Suemasu, Appl.

Phys. Lett. **104**, 252104 (2014).

[65] D. Tsukahara, S. Yachi, H. Takeuchi, R. Takabe, W. Du, M. Baba, Y. Li, K. Toko, N. Usami, and T. Suemasu, Appl. Phys. Lett. **108**, 152101 (2016).

[66] M. Takeishi, Y. Matsumoto, R. Sasaki, T. Saito, and T. Suemasu, Physics Procedia **11**, 27 (2011).

[67] R. Takabe, M. Baba, K. Nakamura, W. Du, M. A. Khan, S. Koike, K. Toko, K. O. Hara, N. Usami, and T. Suemasu, Phys. Status Solidi C **10**, 1753 (2013).

[68] K. Nakamura, M. Baba, M. Ajmal Khan, W. Du, M. Sasase, K. O. Hara, N. Usami, K. Toko, and T. Suemasu, J. Appl. Phys. **113**, 053511 (2013).

[69] A. D. Le Claire, Br. J. Appl. Phys. **14**, 351 (1963).

[70] N. Zhang, K. Nakamura, M. Baba, K. Toko, and T. Suemasu, Jpn. J. Appl. Phys. **53**, 04ER02 (2014).

[71] R. Vismara, O. Isabella, and M. Zeman, Proc. of SPIE **9898**, 98980J (2016).

[72] K. O. Hara, N. Usami, K. Toh, M. Baba, K. Toko, and T. Suemasu, J. Appl. Phys. **112**, 083108 (2012).

[73] K. O. Hara, N. Usami, K. Nakamura, R. Takabe, M. Baba, K. Toko, and T. Suemasu, Phys. Stat. Solidi C **10**, 1677 (2013).

[74] K. O. Hara, N. Usami, K. Nakamura, R. Takabe, M. Baba, K. Toko, and T. Suemasu,

Appl. Phys. Express **6**, 112302 (2013).

[75] T. Daud, K. M. Koliwad, and F. G. Allen, Appl. Phys. Lett. **33**, 1009 (1978).

[76] K. Watanabe, T. Nokuo, J. Chen, and T. Sekiguchi, Microscopy **63**, 161 (2014).

[77] R. Takabe, K. O. Hara, M. Baba, W. Du, N. Shimada, K. Toko, N. Usami, and T. Suemasu, J. Appl. Phys. **115**, 193510 (2014).

[78] S. Ueda, Y. Katsuya, M. Tanaka, H. Yoshikawa, Y. Yamashita, S. Ishimaru, Y. Matsushita, and K. Kobayashi, AIP Conf. Proc. **1234**, 403 (2010).

[79] S. Tajima, K. Kataoka, N. Takahashi, Y. Kimoto, T. Fukano, M. Hasegawa, and H. Hazama, Appl. Phys. Lett. **103**, 243906 (2013).

[80] N. Ikeno, Y. Yamashita, H. Oji, S. Miki, K. Arafune, H. Yoshida, S. Satoh, I. Hirosawa, T. Chikyow, and A. Ogura, Jpn. J. Appl. Phys. **54**, 08KD19 (2015).

[81] C. E. ViolBarbosa, C. Shekhar, B. Yan, S. Ouardi, E. Ikenaga, G. H. Fecher, and C. Felser, Phys. Rev. B **88**, 195128 (2013).

[82] R. Takabe, H. Takeuchi, W. Du, K. Ito, K. Toko, S. Ueda, A. Kimura, and T. Suemasu, J. Appl. Phys. **119**, 165304 (2016).

[83] R. Takabe, W. Du, K. Ito, H. Takeuchi, K. Toko, S. Ueda, A. Kimura, and T. Suemasu, J. Appl. Phys. **119**, 025306 (2016).

[84] S. Yachi, R. Takabe, H. Takeuchi, K. Toko, and T. Suemasu, Appl. Phys. Lett. **109**,

072103 (2016).

[85] Z. Zhang, X. Tang, O. Kiowski, M. Hetterich, U. Lemmer, M. Powalla, and H. Hölscher, Appl. Phys. Lett., **100**, 203903 (2012).

[86] I. Visoly-Fisher, S. R. Cohen, and D. Cahen, Appl. Phys. Lett. **82**, 556 (2003).

[87] S. Tsurekawa, K. Kido, and T. Watanabe, Phil. Mag. Lett. **85**, 41 (2005).

[88] S. Honda, T. Mates, B. Rezek, A. Fejfar, and J. Kočka, J. Non. Cryst. Solids **354**, 2310 (2008).

[89] A. Broniatowski, Philos. Mag. B **66**, 767 (1992).

[90] R. Rizk and G. Nouet, Interface Sci. **4**, 303 (1997).

[91] J. Chen, T. Sekiguchi, R. Xie, P. Ahmet, T. Chikyo, D. Yang, S. Ito, and F. Yin, Scripta Mater., **52**, 1211 (2005).

[92] S. Tsurekawa, H. Takahashi, Y. Nishibe, and T. Watanabe, Phil. Mag. **93**, 1413 (2013).

[93] M. Baba, K. O. Hara, D. Tsukahara, K. Toko, N. Usami, T. Sekiguchi, and T. Suemasu, J. Appl. Phys. **116** , 235301 (2014).

[94] D. Tsukahara, M. Baba, S. Honda, Y. Imai, K. O. Hara, N. Usami, K. Toko, J. H. Werner, and T. Sueamsu, J. Appl. Phys. **116** , 123709 (2014).

[95] M. Baba, M. Kohyama, and T. Suemasu, J. Appl. Phys. **120**, 085311 (2016).

[96] T. Suemasu, Jpn. J. Appl. Phys. **54**, 07JA01 (2015).

[97] T. Suemasu, K. Morita, M. Kobayashi, M. Saida, and M. Sasaki, Jpn. J. Appl. Phys. **45**, L519 (2006).

[98] R. Takabe, S. Yachi, W. Du, D. Tsukahara, H. Takeuchi, K. Toko, and T. Suemasu, AIP Advances **6**, 085107 (2016).

[99] S. Yachi, R. Takabe, K. Toko, and T. Sueamasu, Asia-Pacific Conference on Semiconducting Silicides and Related Materials, 17-P8, Fukuoka, Japan, July 17, 2016.

[100] R. Takabe, S. Yachi, K. Toko, and T. Suemasu, Fall Meeting of the Japan Society of Applied Physics, 15p-B3-10, Niigata, Japan, September 15, 2016.

[101] Y. Imai, M. Sohma, and T. Suemasu, Jpn. J. Appl. Phys. **54**, 07JE03 (2015).

[102] Y. Inomata, T. Suemasu, T. Izawa, and F. Hasegawa, Jpn. J. Appl. Phys. **43**, L771 (2004).

[103] K. Morita, M. Kobayashi, and T. Suemasu, Jpn. J. Appl. Phys. **45**, L390 (2006).

[104] T. Suemasu, K. Morita, M. Kobayashi, and Y. Ichikawa, Phys. Procedia **23**, 53 (2012).

[105] M. Imai, A. Sato, T. Aoyagi, T. Kimura, and Y. Mori, Intermetallics **18**, 548 (2010).

[106] Y. Imai and A. Watanabe, Thin Solid Films **515**, 8219 (2007).

[107] Y. Imai and A. Watanabe, Intermetallics **18**, 1432 (2010).

Table 1. Calculated electronic energies for impurity-doped $BaSi_2$.

Compound	Total energy (eV)
$Ba_8Si_{16} + B \rightarrow Ba_7B^{(1)}Si_{16} + Ba$	−132.758 (−130.846 −1.912)
$Ba_8Si_{16} + B \rightarrow Ba_8B^{(3)}Si_{15} + Si$	−138.209 (−132.792 −5.417)
$Ba_8Si_{16} + B \rightarrow Ba_8Si_{16}B$	−138.999
$Ba_8Si_{16} + Al \rightarrow Ba_7Al^{(1)}Si_{16} + Ba$	−130.609 (−128.697 −1.912)
$Ba_8Si_{16} + Al \rightarrow Ba_8Al^{(3)}Si_{15} + Si$	−136.494 (−131.077 −5.417)
$Ba_8Si_{16} + Al \rightarrow Ba_8Si_{16}Al$	−135.698
$Ba_8Si_{16} + In \rightarrow Ba_7In^{(1)}Si_{16} + Ba$	−130.420 (−128.508 −1.912)
$Ba_8Si_{16} + In \rightarrow Ba_8In^{(3)}Si_{15} + Si$	−135.586 (−130.169 −5.417)
$Ba_8Si_{16} + In \rightarrow Ba_8Si_{16}In$	−133.857
$Ba_8Si_{16} + Ga \rightarrow Ba_7Ga^{(1)}Si_{16} + Ba$	−130.457 (−128.545 −1.912)
$Ba_8Si_{16} + Ga \rightarrow Ba_8Ga^{(3)}Si_{15} + Si$	−136.199 (−130.782 −5.417)
$Ba_8Si_{16} + Ga \rightarrow Ba_8Si_{16}Ga$	−135.533
$Ba_8Si_{16} + N \rightarrow Ba_7N^{(1)}Si_{16} + Ba$	−134.100 (−132.188 −1.912)
$Ba_8Si_{16} + N \rightarrow Ba_8N^{(3)}Si_{15} + Si$	−141.279 (−135.862 −5.417)
$Ba_8Si_{16} + N \rightarrow Ba_8Si_{16}N$	−141.932

$Ba_8Si_{16} + P \rightarrow Ba_7P^{(1)}Si_{16} + Ba$	□	−132.603 (−130.691 −1.912)
$Ba_8Si_{16} + P \rightarrow Ba_8P^{(3)}Si_{15} + Si$	□	−139.472 (−134.050 −5.417)
$Ba_8Si_{16} + P \rightarrow Ba_8Si_{16}P$	□	−135.698
$Ba_8Si_{16} + As \rightarrow Ba_7As^{(1)}Si_{16} + Ba$		−132.025 (−130.113 −1.912)
$Ba_8Si_{16} + As \rightarrow Ba_8As^{(3)}Si_{15} + Si$	□	−138.577 (−133.160 −5.417)
$Ba_8Si_{16} + As \rightarrow Ba_8Si_{16}As$	□	−137.433
$Ba_8Si_{16} + Sb \rightarrow Ba_7Sb^{(1)}Si_{16} + Ba$		−131.301 (−129.389 −1.912)
$Ba_8Si_{16} + Sb \rightarrow Ba_8Sb^{(3)}Si_{15} + Si$		−137.690 (−132.273 −5.417)
$Ba_8Si_{16} + Sb \rightarrow Ba_8Si_{16}Sb$		−135.861
$Ba_8Si_{16} + O \rightarrow Ba_7O^{(1)}Si_{16} + Ba$	□	−134.378 (−132.466 −1.912)
$Ba_8Si_{16} + O \rightarrow Ba_8O^{(3)}Si_{15} + Si$	□	−140.857 (−135.440 −5.417)
$Ba_8Si_{16} + O \rightarrow Ba_8Si_{16}O$		−141.494

Table 2. Experimental results of impurity-doped $BaSi_2$. The carrier concentrations in this table are the highest values ever reported.

Group 13	Group 15
B (p ~ 10^{20} cm^{-3})[58,63-65]	N (under investigation)
Al (p ~ 4×10^{17} cm^{-3}) [66]	As (n ~ $2\times10^{17}$$cm^{-3}$) [61]
Ga (n-type) [62]	P (n ~ 10^{18} cm^{-3}) [59,60,67]
In (p ~ 5×10^{17} cm^{-3}) [54]	Sb (n ~ 10^{20} cm^{-3}) [54]

Fig. 1 Crystal structure of $BaSi_2$. There are two crystallographically-inequivalent sites for Ba ($Ba^{(1)}$ and $Ba^{(2)}$) and three inequivalent sites for Si ($Si^{(3)}$, $Si^{(4)}$, and $Si^{(5)}$) in the $BaSi_2$ unit cell.

Fig. 2 (a) Partial DOS and (b) band structure of $BaSi_2$.

Fig. 3 Schematic of a two-step growth technique using RDE and MBE for $BaSi_2$.

Fig. 4 (a) RHEED pattern, (b) θ-2θ XRD pattern, (b) pole-figure XRD pattern using asymmetric (301) and (203) diffractions, (d) EBSD crystal orientation map, and (e) schematic of epitaxial variants for *a*-axis-oriented $BaSi_2$ epitaxial film on Si(111)[31]. Panels (a')–(e') are equivalent to the above panels, but for an *a*-axis-oriented $BaSi_2$ epitaxial film on Si(001).

Fig. 5 Possible chemical reactions during the deposition process of $BaSi_2$ on Si by vacuum evaporation of $BaSi_2$ granules.

Fig. 6 Raman spectra for films on Si(111) deposited at various temperatures by vacuum evaporation of $BaSi_2$ granules [34].

Fig. 7 θ-2θ XRD patterns for $BaSi_2$ films grown on SiO_2 at 500, 550, and 600 °C by RF sputtering [49].

Fig. 8 Temperature dependence of electron mobility in intrinsically doped n-$BaSi_2$ grown by MBE. The n is 5×10^{15} cm^{-3} at 300 K. Broken lines are a guide to eyes.

Fig. 9 Total DOSs of (a) $Ba_8Si_{15}B^{(3)}$, (b) $Ba_8Si_{16}B$, (c) $Ba_8Si_{15}Al^{(3)}$, (d) $Ba_8Si_{15}In^{(3)}$, (e) $Ba_8Si_{15}Ga^{(3)}$, (f) $Ba_8Si_{16}O$, (g) $Ba_8Si_{15}N^{(3)}$, (h) $Ba_8Si_{15}P^{(3)}$, (i) $Ba_8Si_{15}As^{(3)}$, and (j) $Ba_8Si_{15}Sb^{(3)}$ [94].

Fig. 10 (a) Measured and simulated SIMS profiles of B for a $BaSi_2$ sample capped with a 180 nm thick B layer that was annealed at 800 °C for 1 h [68]. (b) Arrhenius plots for the lattice diffusion coefficient D_l and the product of the segregation factor and DB diffusion coefficient sD_{GB} of Sb, As, B and other atoms [70].

Fig. 11 (a) Absorption spectrum and (b) $(\alpha dhv)^{1/2}$ versus hv plot for $BaSi_2$ epitaxial layers on transparent Si(111) [17].

Fig. 12 Wavelength dependence of refractive index n_{index} and extinction coefficient κ of $BaSi_2$ measured on a 150 nm thick $BaSi_2$ epitaxial layer on Si(111) by MBE. Reprinted with permission from [71] R. Vismara, O. Isabella, and M. Zeman, "Organometallic Halide Perovskite / Barium Di-Silicide Thin-Film Double-Junction Solar Cells," Proc. of SPIE **9898**, 98980J (2016).

Fig. 13 (a) Photoconductivity decay curves of a $BaSi_2$ film with laser intensities of (A) 1.3×10^5, (B) 1.3×10^4, (C) 1.1×10^3, and (D) 1.1×10^2 [72]. (b) Dependence of the inverse of the carrier lifetime on the inverse of $BaSi_2$ layer thickness [74].

Fig. 14 Panel (a) shows SE and panel (a') EBIC images around the Al/n-$BaSi_2$ Schottky junction on Si(111). Panels (b) and (b') show the same measurements around the Pt/n-$BaSi_2$ Schottky junction on Si(001). (c) Experimental and simulated (solid lines) EBIC line-scan profiles along the dotted lines from points A to A' in panel (a') and B to B' in panel (b') [19]. Plan-view TEM images of $BaSi_2$ on (d) Si(111) and (d') Si(001).

Fig. 15 Dependence of minority-carrier lifetime and minority-carrier diffusion length on p.

Fig. 16 TEM cross sections of (a) a-Si/$BaSi_2$ and (b) native-oxide/$BaSi_2$ [82].

Fig. 17 Ba $3d_{5/2}$ core-level HAXPES spectra for (a) a-Si(5 nm)/$BaSi_2$(730 nm), (b) normalized spectra of (a), and (c) oxide(ca. 8 nm)/$BaSi_2$(600 nm) taken at TOA = 15°, 30°, and 90°. The spectrum measured at TOA = 15º in (b) and the spectra measured at TOA = 30° and 90° in (c) can be fitted by the sum of two Gaussian curves (dashed lines). Si 2s core-level HAXPES spectra for (a') a-Si(5 nm)/$BaSi_2$(730 nm), (b') normalized spectra of (a'), and (c') oxide(ca. 8 nm)/$BaSi_2$(600 nm) taken at TOA = 15° , 30° , and 90° . The spectra measured at TOA = 30° and 90° in panel (c') can be reconstructed by the sum of two Gaussian curves (dashed lines) [82].

Fig. 18 Valence-band alignment between native-oxide, $BaSi_2$, and a-Si.

Fig. 19 Photoresponse and reflectance spectra of samples (a) without and (b) with a 3 nm

thick a-Si capping layer [84]. The bias voltages were applied so that the photogenerated minority carriers (holes) in n-$BaSi_2$ were transferred to the surface electrode (ITO) across the a-Si/n-$BaSi_2$ or native-oxide/n-$BaSi_2$ interface [84].

Fig. 20 AFM topographic and (b) KFM electrostatic potential images with their cross sections along the white lines for undoped n-$BaSi_2$ on Si(111). The observed area is 5 × 5 μm^2. (c) Band lineup around GBs for $BaSi_2$, and (d) histogram of barrier height at GBs [23].

Fig. 21 (a) AFM topographic and (b) KFM electrostatic potential images with their cross sections along the white lines AA', parallel to Si[110], and BB', parallel to Si[1-10], for undoped n-$BaSi_2$ on Si(001). (c) Band lineup around GBs for $BaSi_2$, and (d) histograms of barrier height at GBs along Si[110] and along Si[1-10] [23].

Fig. 22 (a) Expected band alignment at the p-$BaSi_2$/n-Si heterojunction. Owing to the difference in the carrier concentration between the p-$BaSi_2$ ($p = 2.2 \times 10^{18} cm^{-3}$) and n-Si ($n = 2 \times 10^{15} cm^{-3}$), the depletion region stretches into the n-Si region. (b) TEM cross section of the a-Si(4 nm)/p-$BaSi_2$(20 nm)/n-Si heterojunction [65].

Fig. 23 (a) *J-V* curves under AM1.5 illumination. p-$BaSi_2$ layer thickness was varied as10, 15, 20, 30, and 50 nm [99]. (b) *EQE*, *IQE*, and *R* spectra of the p-$BaSi_2$(20 nm)/n-Si heterojunction solar cell. The contributions of $BaSi_2$ and Si are also denoted by *EQE*($BaSi_2$) and *EQE*(Si), respectively.

Fig. 24 Dependence of solar cell parameters such as η, V_{OC}, J_{SC}, and *FF* on p-$BaSi_2$ layer thickness. *p* was set to approximately 2×10^{18} cm^{-3} [99].

Fig. 25 Time evolution of η of p-$BaSi_2$(20 nm)/n-Si solar cells, capped with a 2 nm or 3 nm thick a-Si [100]. *p* was set to approximately 2×10^{18} cm^{-3}.

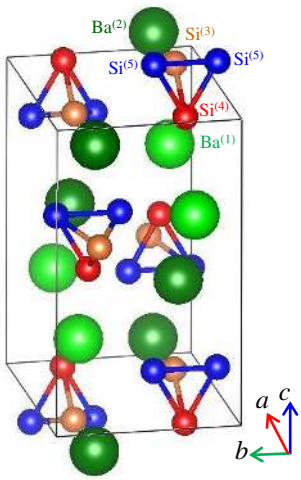

Fig. 1

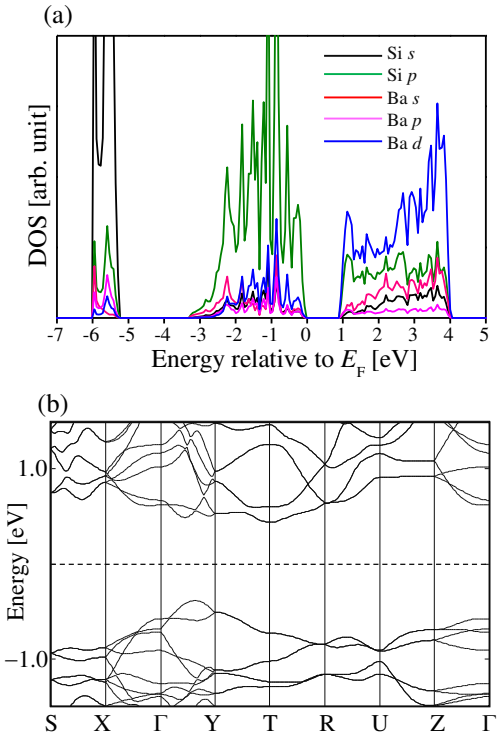
(a)
Si s
Si p
Ba s
Ba p
Ba d
DOS [arb. unit]
-7 -6 -5 -4 -3 -2 -1 0 1 2 3 4 5
Energy relative to E_F [eV]
(b)
1.0
−1.0
Energy [eV]
S X Γ Y T R U Z Γ

Fig. 2

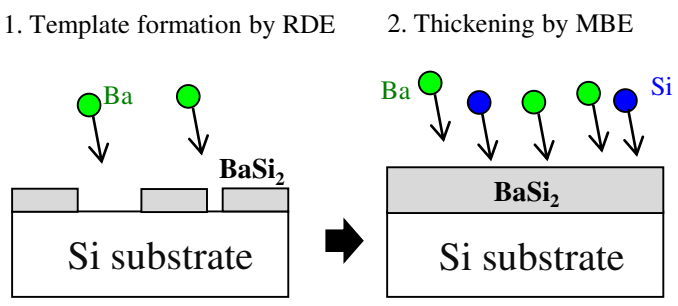
1. Template formation by RDE
2. Thickening by MBE
Ba
BaSi2
Si substrate
Ba
Si
BaSi2
Si substrate

Fig. 3

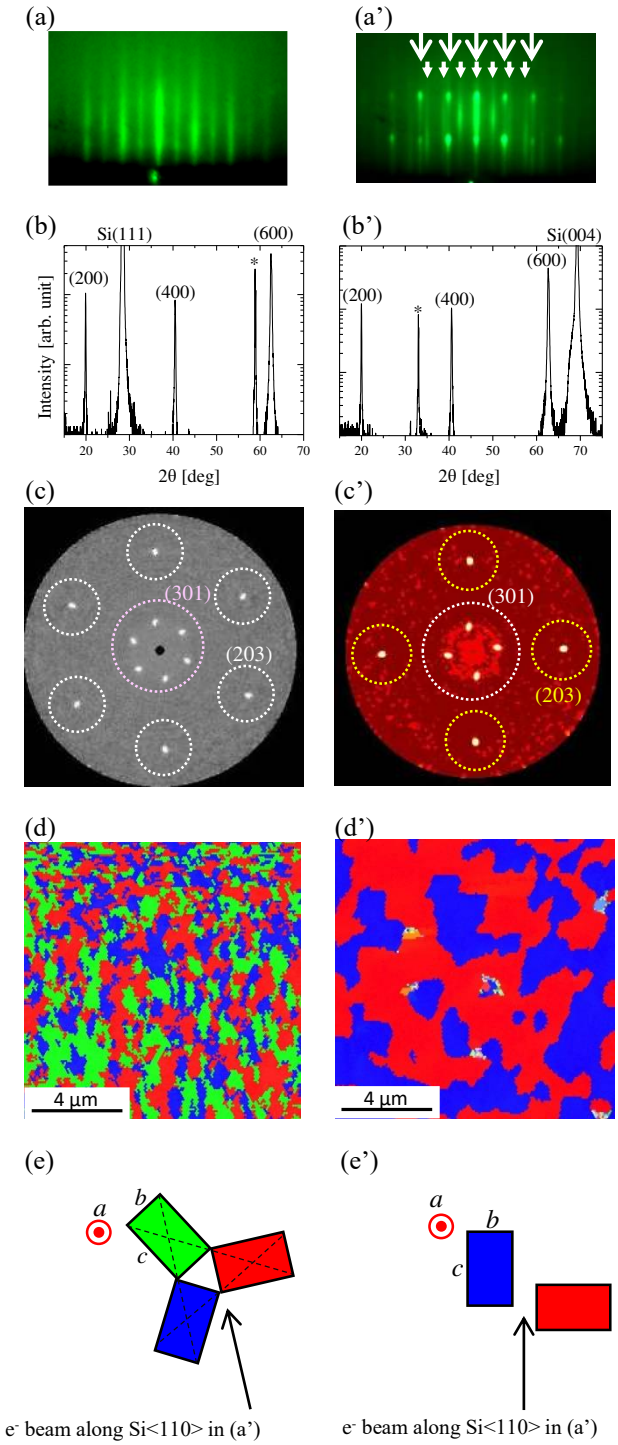
(a)
(a')
(b)
Si(111)
(600)
(200)
(400)
*
Intensity [arb. unit]
20 30 40 50 60 70
2θ [deg]
(b')
Si(004)
(600)
(200)
*
(400)
20 30 40 50 60 70
2θ [deg]
(c)
(301)
(203)
(c')
(301)
(203)
(d)
4 μm
(d')
4 μm
(e)
a
b
c
e⁻ beam along Si<110> in (a')
(e')
a
b
c
e⁻ beam along Si<110> in (a')

Fig. 4

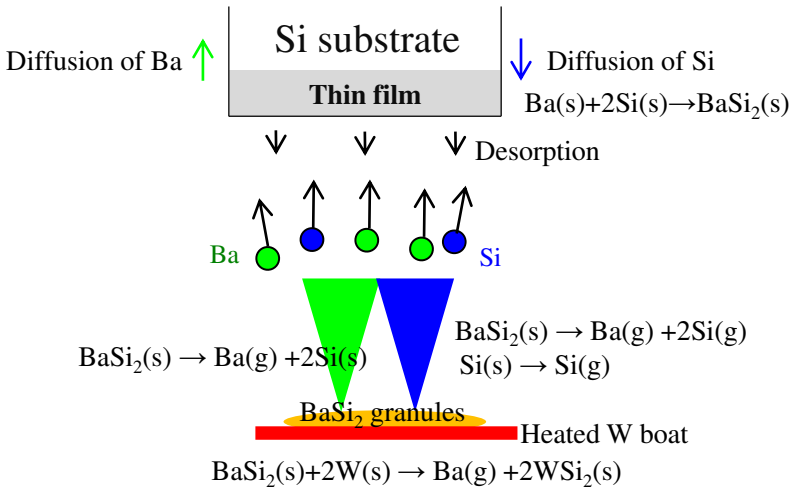
Si substrate
Thin film
Diffusion of Ba
Diffusion of Si
Ba(s)+2Si(s)→BaSi2(s)
Desorption
Ba
Si
BaSi2(s) → Ba(g) +2Si(s)
BaSi2(s) → Ba(g) +2Si(g)
Si(s) → Si(g)
BaSi2 granules
Heated W boat
BaSi2(s)+2W(s) → Ba(g) +2WSi2(s)

Fig. 5

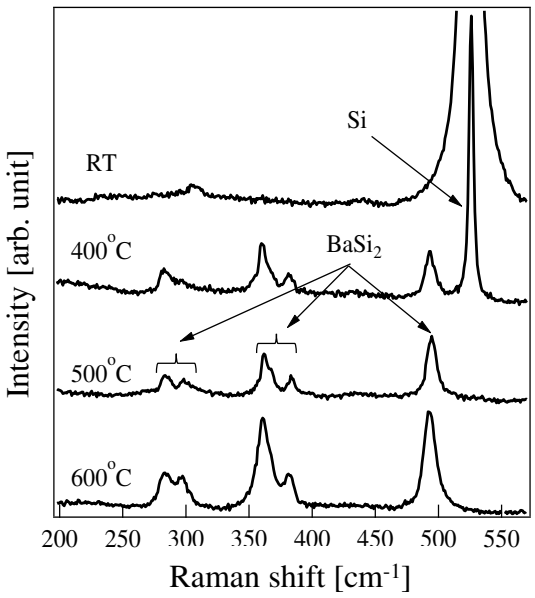
Si
RT
400°C
BaSi2
500°C
600°C
Intensity [arb. unit]
200
250
300
350
400
450
500
550
Raman shift [cm-1]

Fig. 6

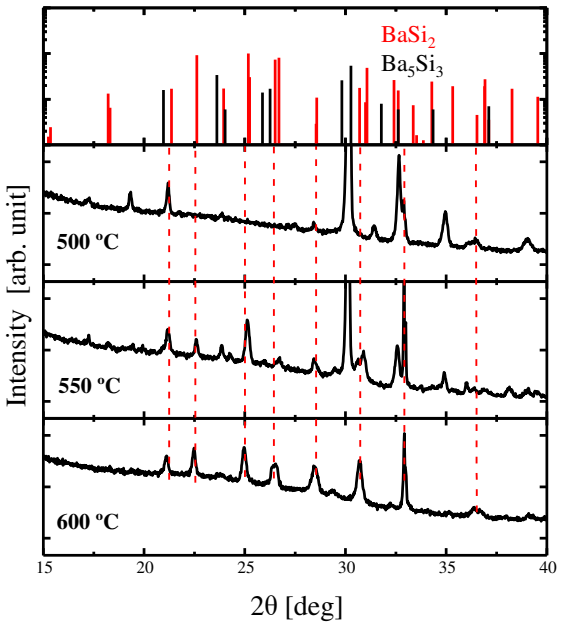
BaSi2
Ba5Si3
500 ºC
550 ºC
600 ºC
Intensity [arb. unit]
15
20
25
30
35
40
2θ [deg]

Fig. 7

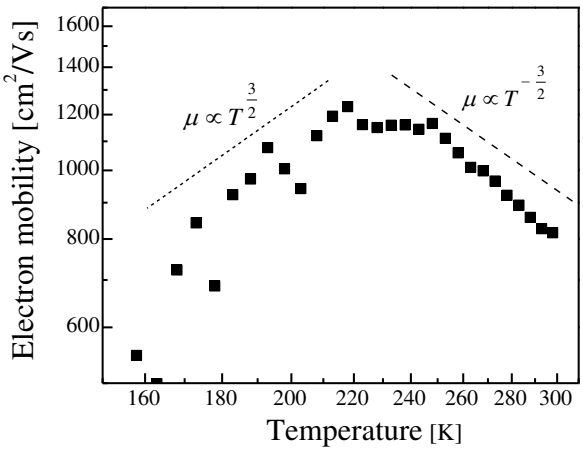
Electron mobility [cm²/Vs]
1600
1400
1200
1000
800
600
160
180
200
220
240
260
280
300
Temperature [K]
$\mu \propto T^{\frac{3}{2}}$
$\mu \propto T^{-\frac{3}{2}}$

Fig. 8

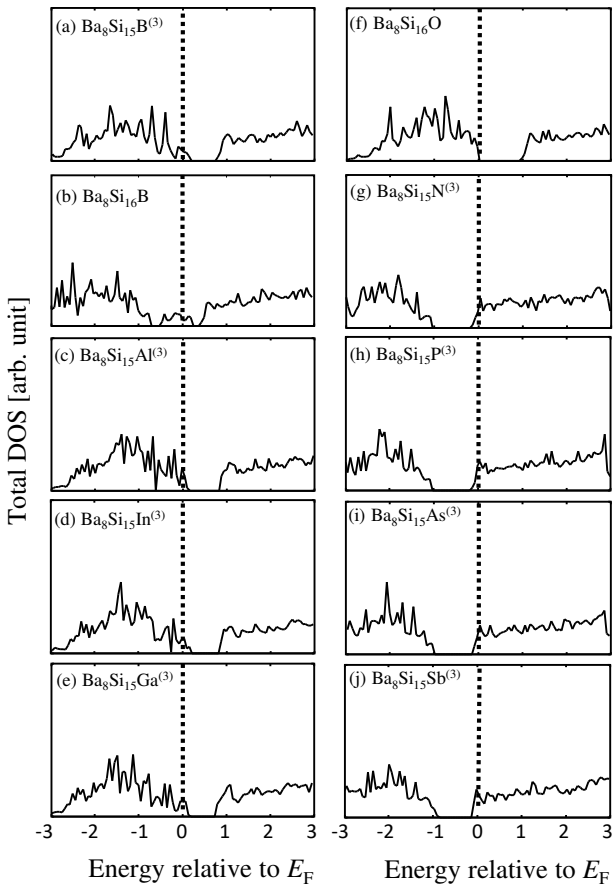
(a) $Ba_8Si_{15}B^{(3)}$
(b) $Ba_8Si_{16}B$
(c) $Ba_8Si_{15}Al^{(3)}$
(d) $Ba_8Si_{15}In^{(3)}$
(e) $Ba_8Si_{15}Ga^{(3)}$
(f) $Ba_8Si_{16}O$
(g) $Ba_8Si_{15}N^{(3)}$
(h) $Ba_8Si_{15}P^{(3)}$
(i) $Ba_8Si_{15}As^{(3)}$
(j) $Ba_8Si_{15}Sb^{(3)}$
Total DOS [arb. unit]
-3 -2 -1 0 1 2 3
Energy relative to E_F
Energy relative to E_F

Fig. 9

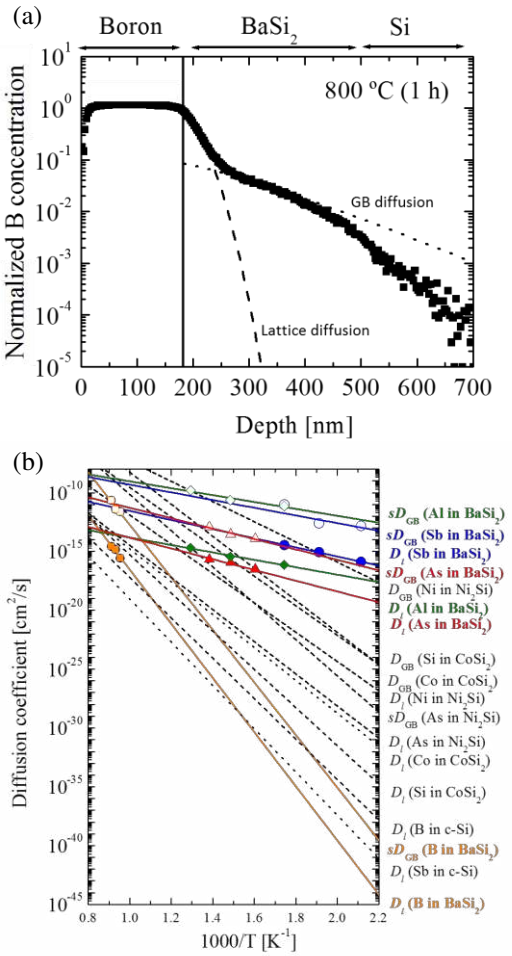
(a)
Boron
BaSi2
Si
800 ºC (1 h)
GB diffusion
Lattice diffusion
Normalized B concentration
Depth [nm]
(b)
Diffusion coefficient [cm2/s]
1000/T [K-1]
sDGB (Al in BaSi2)
sDGB (Sb in BaSi2)
Dl (Sb in BaSi2)
sDGB (As in BaSi2)
DGB (Ni in Ni2Si)
Dl (Al in BaSi2)
Dl (As in BaSi2)
DGB (Si in CoSi2)
DGB (Co in CoSi2)
Dl (Ni in Ni2Si)
sDGB (As in Ni2Si)
Dl (As in Ni2Si)
Dl (Co in CoSi2)
Dl (Si in CoSi2)
Dl (B in c-Si)
sDGB (B in BaSi2)
Dl (Sb in c-Si)
Dl (B in BaSi2)

Fig. 10

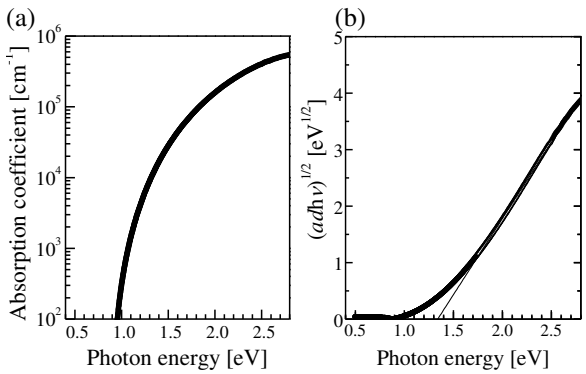
(a)
Absorption coefficient [cm^{-1}]
10^6
10^5
10^4
10^3
10^2
0.5
1.0
1.5
2.0
2.5
Photon energy [eV]
(b)
$(\alpha d h\nu)^{1/2}$ [eV$^{1/2}$]
5
4
3
2
1
0
0.5
1.0
1.5
2.0
2.5
Photon energy [eV]

Fig. 11

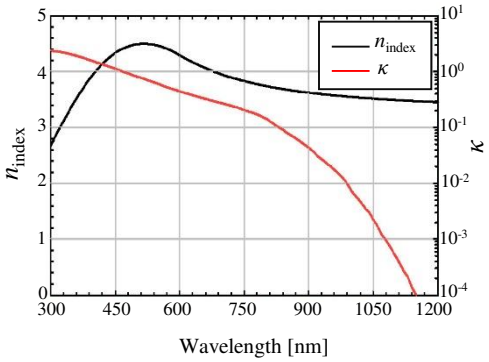
n_{index}
κ
n_{index}
κ
Wavelength [nm]
0
1
2
3
4
5
300
450
600
750
900
1050
1200
10^{1}
10^{0}
10^{-1}
10^{-2}
10^{-3}
10^{-4}

Fig. 12

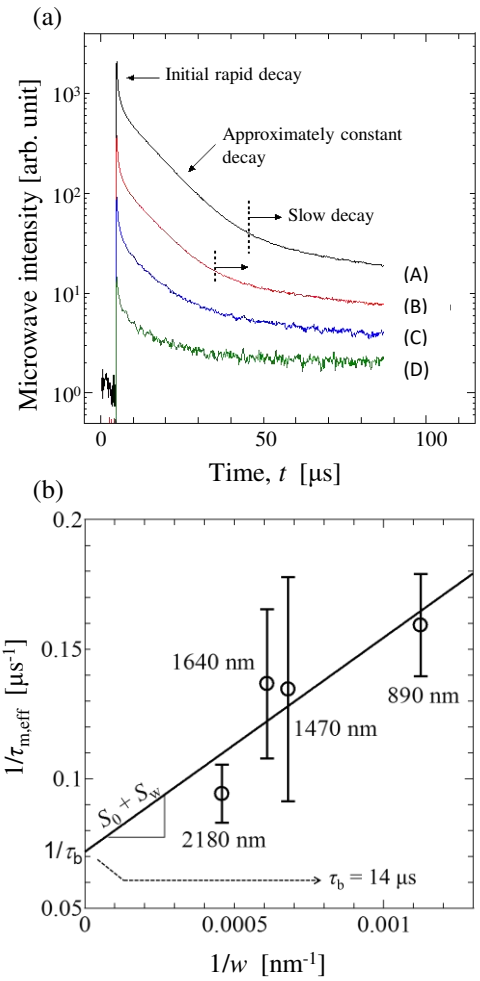
(a)
Initial rapid decay
Approximately constant decay
Slow decay
(A)
(B)
(C)
(D)
Microwave intensity [arb. unit]
Time, t [μs]
(b)
1640 nm
1470 nm
890 nm
2180 nm
$S_0 + S_w$
$1/\tau_b$
τ_b = 14 μs
$1/\tau_{m,eff}$ [μs^{-1}]
$1/w$ [nm^{-1}]

Fig. 13

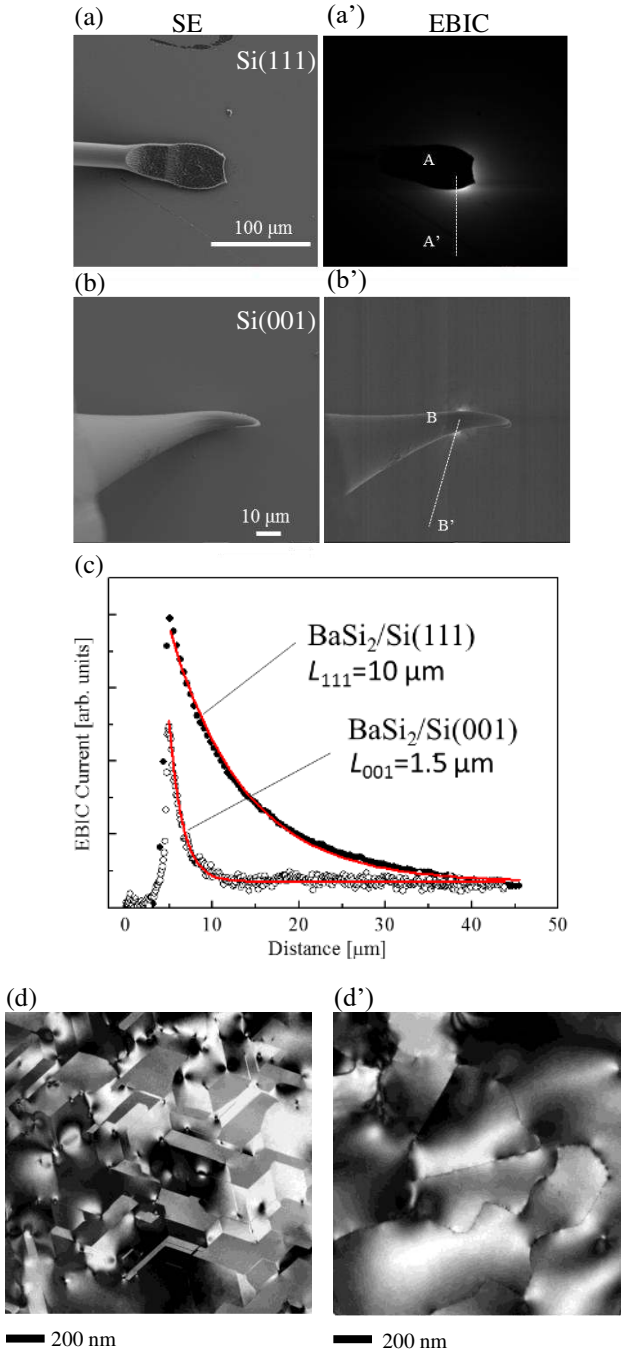
(a)
SE
(a')
EBIC
Si(111)
100 μm
A
A'
(b)
(b')
Si(001)
10 μm
B
B'
(c)
EBIC Current [arb. units]
BaSi2/Si(111)
L111=10 μm
BaSi2/Si(001)
L001=1.5 μm
0
10
20
30
40
50
Distance [μm]
(d)
(d')
200 nm
200 nm

Fig. 14

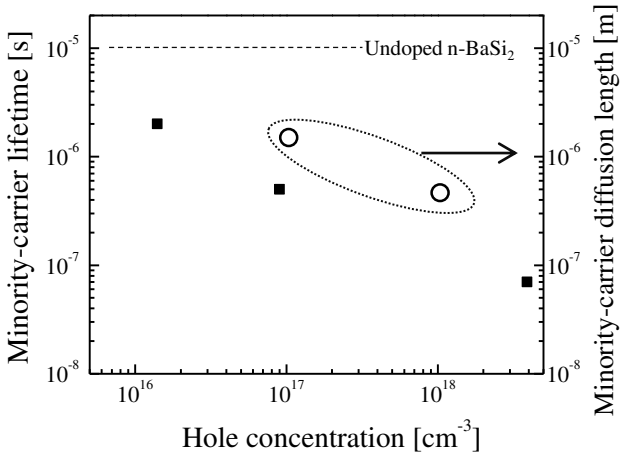
Undoped n-BaSi2
Minority-carrier lifetime [s]
Minority-carrier diffusion length [m]
Hole concentration [cm-3]
10-5
10-6
10-7
10-8
1016
1017
1018

Fig. 15

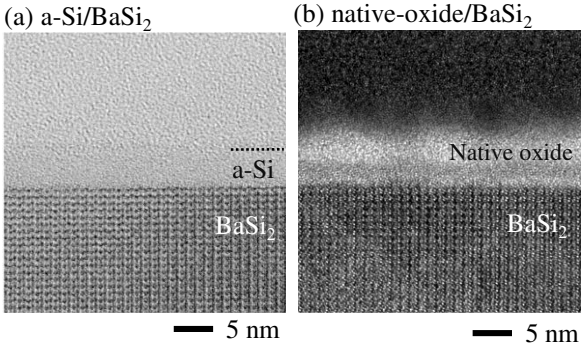
(a) a-Si/BaSi2
a-Si
BaSi2
5 nm
(b) native-oxide/BaSi2
Native oxide
BaSi2
5 nm

Fig. 16

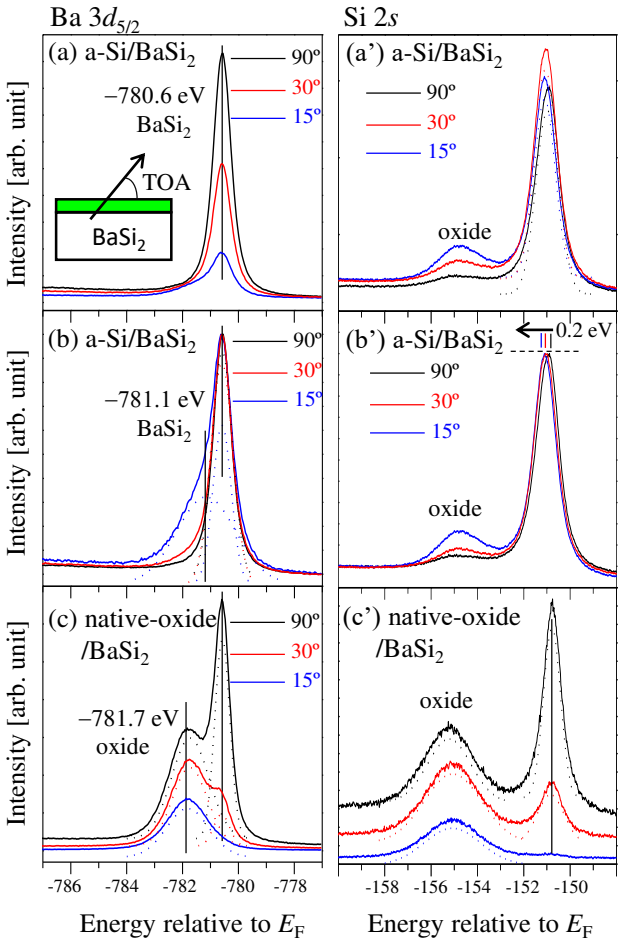
Ba 3$d_{5/2}$
Si 2s
(a) a-Si/BaSi$_2$
90°
30°
15°
−780.6 eV
BaSi$_2$
TOA
BaSi$_2$
(a') a-Si/BaSi$_2$
oxide
(b) a-Si/BaSi$_2$
−781.1 eV
BaSi$_2$
(b') a-Si/BaSi$_2$
0.2 eV
(c) native-oxide /BaSi$_2$
−781.7 eV
oxide
(c') native-oxide /BaSi$_2$
Intensity [arb. unit]
-786 -784 -782 -780 -778
-158 -156 -154 -152 -150
Energy relative to E_F

Fig. 17

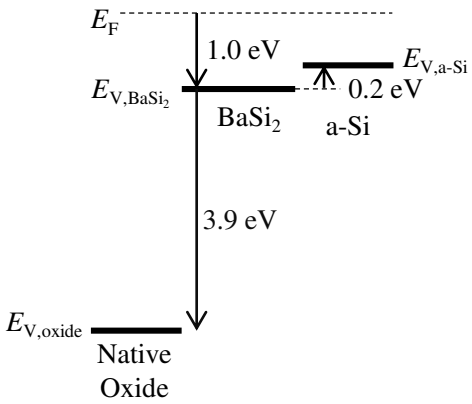
E_F
1.0 eV
$E_{V,a\text{-}Si}$
$E_{V,BaSi_2}$
0.2 eV
$BaSi_2$
a-Si
3.9 eV
$E_{V,oxide}$
Native
Oxide

Fig. 18

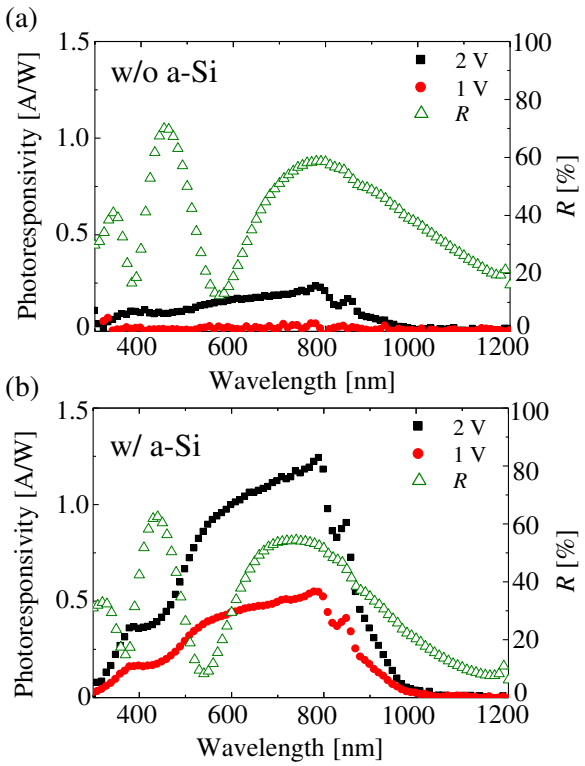
(a)
w/o a-Si
2 V
1 V
R
Photoresponsivity [A/W]
R [%]
Wavelength [nm]
(b)
w/ a-Si
2 V
1 V
R
Photoresponsivity [A/W]
R [%]
Wavelength [nm]

Fig. 19

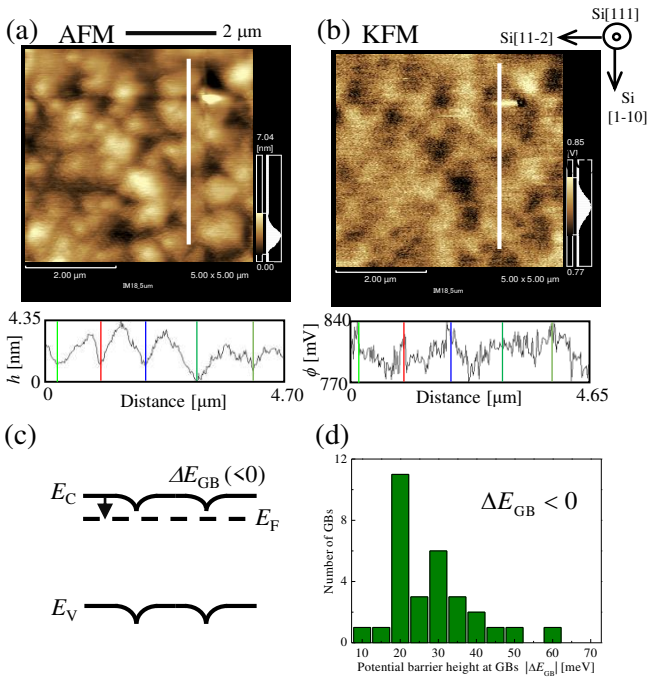
(a) AFM
2 μm
7.04
[nm]
0.00
2.00 μm
5.00 x 5.00 μm
(b) KFM
Si[111]
Si[11-2]
Si
[1-10]
0.85
[V]
0.77
2.00 μm
5.00 x 5.00 μm
4.35
h [nm]
0
0
Distance [μm]
4.70
840
φ [mV]
770
0
Distance [μm]
4.65
(c)
ΔE_GB (<0)
E_C
E_F
E_V
(d)
ΔE_GB < 0
Number of GBs
12
8
4
0
10
20
30
40
50
60
70
Potential barrier height at GBs |ΔE_GB| [meV]

Fig. 20

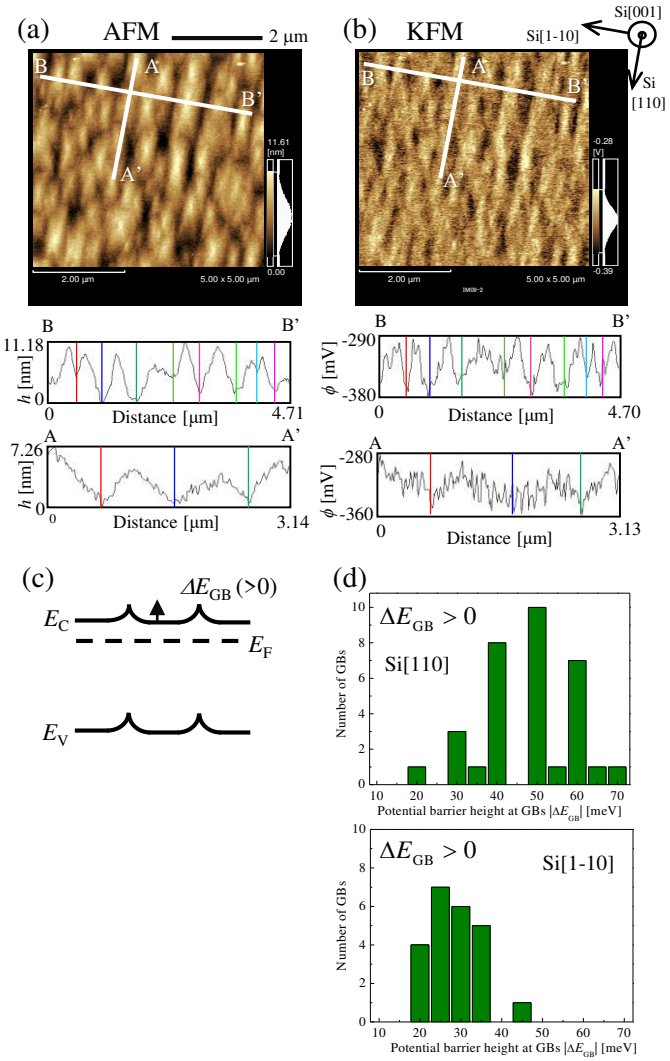
(a)
AFM
2 μm
B
A
B'
A'
11.61
[nm]
0.00
2.00 μm
5.00 x 5.00 μm
(b)
KFM
Si[001]
Si[1-10]
Si
[110]
-0.28
[V]
-0.39
B
11.18
h [nm]
0
0
Distance [μm]
4.71
-290
-380
ϕ [mV]
4.70
A
7.26
3.14
-280
-360
3.13

(c)
ΔE_GB (>0)
E_C
E_F
E_V
(d)
ΔE_GB > 0
Si[110]
Number of GBs
Potential barrier height at GBs |ΔE_GB| [meV]
Si[1-10]

Fig. 21

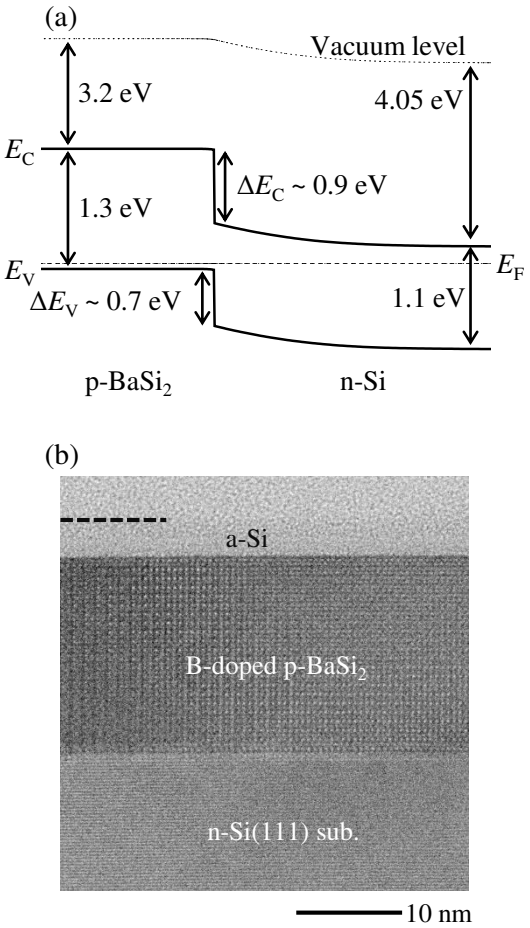
(a)
Vacuum level
3.2 eV
4.05 eV
E_C
ΔE_C ~ 0.9 eV
1.3 eV
E_V
E_F
ΔE_V ~ 0.7 eV
1.1 eV
p-$BaSi_2$
n-Si
(b)
a-Si
B-doped p-$BaSi_2$
n-Si(111) sub.
10 nm

Fig. 22

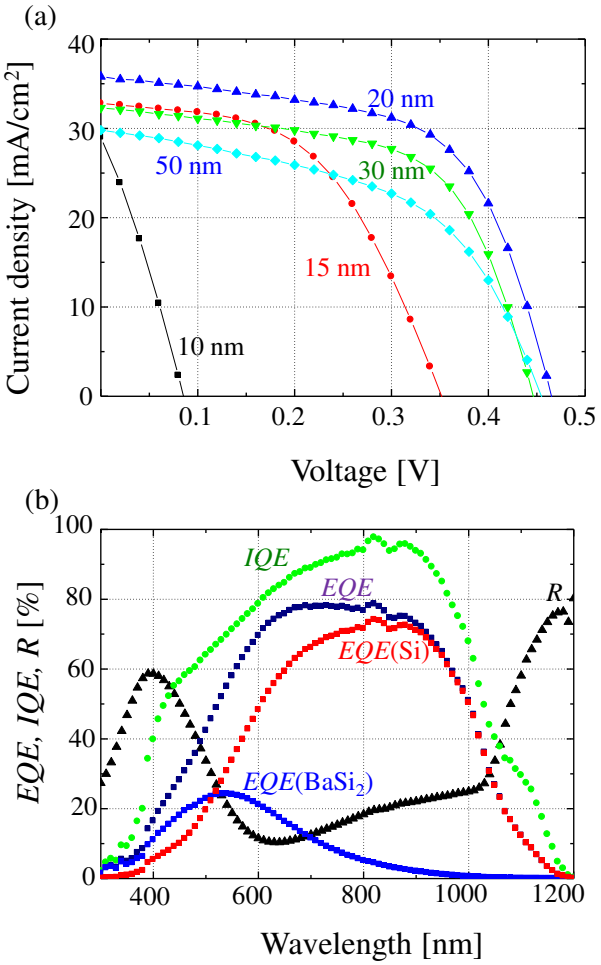
(a)
Current density [mA/cm^2]
Voltage [V]
20 nm
30 nm
50 nm
15 nm
10 nm
(b)
EQE, IQE, R [%]
Wavelength [nm]
IQE
EQE
R
EQE(Si)
EQE(BaSi$_2$)

Fig. 23

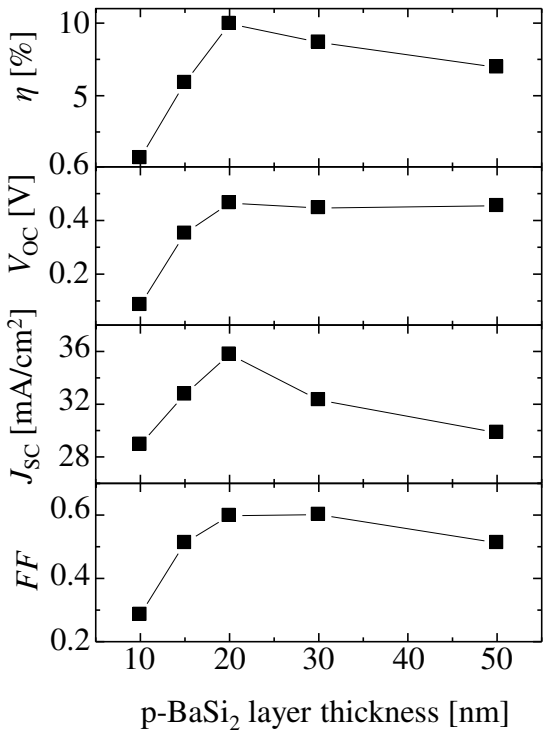
η [%]
10
5
0.6
V_{OC} [V]
0.4
0.2
J_{SC} [mA/cm^2]
36
32
28
FF
0.6
0.4
0.2
10
20
30
40
50
p-BaSi$_2$ layer thickness [nm]

Fig. 24

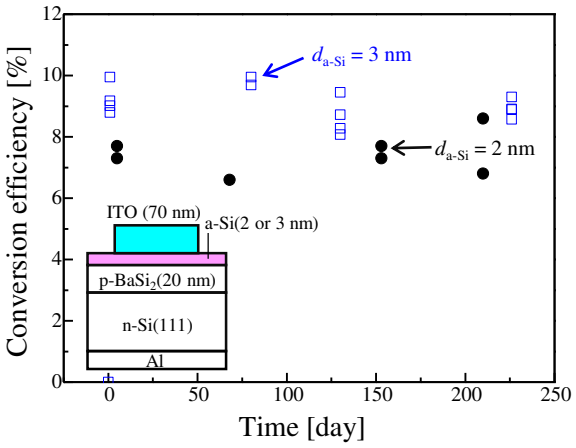
Conversion efficiency [%]
Time [day]
$d_{a\text{-}Si}$ = 3 nm
$d_{a\text{-}Si}$ = 2 nm
ITO (70 nm)
a-Si(2 or 3 nm)
p-BaSi$_2$(20 nm)
n-Si(111)
Al

Fig. 25